

## Research Paper

# Visualization and quantification of *in vivo* homing kinetics of myeloid-derived suppressor cells in primary and metastatic cancer

Sabrina H. L. Hoffmann<sup>1</sup>, Dorothea I. Reck<sup>1</sup>, Andreas Maurer<sup>1,2</sup>, Birgit Fehrenbacher<sup>3</sup>, Jaclyn E. Sceneay<sup>4</sup>, Marilena Poxleitner<sup>1</sup>, Hasan H. Öz<sup>5</sup>, Walter Ehrlichmann<sup>1</sup>, Gerald Reischl<sup>1,2</sup>, Kerstin Fuchs<sup>1</sup>, Martin Schaller<sup>3</sup>, Dominik Hartl<sup>5</sup>, Manfred Kneilling<sup>1,2,3</sup>, Andreas Möller<sup>4</sup>, Bernd J. Pichler<sup>1,2,6</sup> and Christoph M. Griessinger<sup>1</sup>

1. Werner Siemens Imaging Center, Department of Preclinical Imaging and Radiopharmacy, Eberhard Karls University Tübingen, Tübingen, Germany
2. iFIT-Cluster of Excellence, University of Tübingen, Germany
3. Department of Dermatology, Eberhard Karls University Tübingen, Tübingen, Germany
4. Tumor Microenvironment Laboratory, QIMR Berghofer Medical Research Institute, Herston, Australia
5. Children's Hospital, University of Tübingen, Tübingen, Germany
6. German Cancer Consortium (DKTK), Partner Site Tübingen; German Cancer Research Center (DKFZ), Heidelberg, Germany

✉ Corresponding author: Bernd J. Pichler (bernd.pichler@med.uni-tuebingen.de), Address: Röntgenweg 13, 72076 Tübingen, Germany, Tel: +49 7071 29 83427

© The author(s). This is an open access article distributed under the terms of the Creative Commons Attribution License (<https://creativecommons.org/licenses/by/4.0/>). See <http://ivyspring.com/terms> for full terms and conditions.

Received: 2019.01.18; Accepted: 2019.06.06; Published: 2019.08.12

## Abstract

Myeloid-derived suppressor cells (MDSCs) are immunosuppressive cells of the myeloid compartment and major players in the tumor microenvironment (TME). With increasing numbers of studies describing MDSC involvement in cancer immune escape, cancer metastasis and the dampening of immunotherapy responses, MDSCs are of high interest in current cancer therapy research. Although heavily investigated in the last decades, the *in vivo* migration dynamics of MDSC subpopulations in tumor- or metastases-bearing mice have not yet been studied extensively. Therefore, we have modified our previously reported intracellular cell labeling method and applied it to *in vitro* generated MDSCs for the quantitative *in vivo* monitoring of MDSC migration in primary and metastatic cancer. MDSC migration to primary cancers was further correlated to the frequency of endogenous MDSCs. **Methods:** Utilizing a <sup>64</sup>Cu-labeled 1,4,7-triazacyclononane-triacetic acid (NOTA)-modified CD11b-specific monoclonal antibody (mAb) (clone M1/70), we were able to label *in vitro* generated polymorphonuclear (PMN-) and monocytic (M-) MDSCs for positron emission tomography (PET) imaging. Radiolabeled PMN- and M-MDSCs (<sup>64</sup>Cu]PMN-MDSCs and <sup>64</sup>Cu]M-MDSCs, respectively) were then adoptively transferred into primary and metastatic MMTV-PyMT-derived (PyMT-) breast cancer- and B16F10 melanoma-bearing experimental animals, and static PET and anatomical magnetic resonance (MR) images were acquired 3, 24 and 48 h post cell injection. **Results:** The internalization of the [<sup>64</sup>Cu]NOTA-mAb-CD11b-complex was completed within 3 h, providing moderately stable radiolabeling with little detrimental effect on cell viability and function as determined by Annexin-V staining and T cell suppression in flow cytometric assays. Further, we could non-invasively and quantitatively monitor the migration and tumor homing of both [<sup>64</sup>Cu]NOTA-αCD11b-mAb-labeled PMN- and M-MDSCs in mouse models of primary and metastatic breast cancer and melanoma by PET. We were able to visualize and quantify an increased migration of adoptively transferred [<sup>64</sup>Cu]M-MDSCs than [<sup>64</sup>Cu]PMN-MDSCs to primary breast cancer lesions. The frequency of endogenous MDSCs in the PyMT breast cancer and B16F10 melanoma model correlated to the uptake values of adoptively transferred MDSCs with higher frequencies of PMN- and M-MDSCs in the more aggressive B16F10 melanoma tumors. Moreover, aggressively growing melanomas and melanoma-metastatic lesions recruited higher percentages of both [<sup>64</sup>Cu]PMN- and [<sup>64</sup>Cu]M-MDSCs than primary and metastatic breast cancer lesions as early as 24 h post adoptive MDSC transfer, indicating an overall stronger recruitment of cancer-promoting immunosuppressive MDSCs. **Conclusion:** Targeting of the cell surface integrin CD11b with a radioactive mAb is feasible for labeling of murine MDSCs for PET imaging. Fast internalization of the [<sup>64</sup>Cu]NOTA-αCD11b-mAb provides presumably enhanced stability while cell viability and functionality was not significantly affected. Moreover, utilization of the CD11b-specific mAb allows for straightforward adaptation of the labeling approach for *in vivo* molecular imaging of other myeloid cells of interest in cancer therapy, including monocytes, macrophages or neutrophils.

Key words: Myeloid-derived suppressor cells, cancer, cell tracking, positron emission tomography

## Introduction

While cancer treatment options are constantly being improved, metastatic disease is still often

deemed incurable, accounting for approximately 90% of cancer-related deaths [1-3]. Due to their potent

immunosuppressive capacity, and apparent involvement in cancer progression and metastasis, myeloid-derived suppressor cells (MDSCs) have moved into the focus of cancer research. MDSCs are considered aberrantly activated immature cells of the myeloid compartment, whose expansion is mediated primarily by granulocyte-macrophage colony stimulation factor (GM-CSF), macrophage CSF (M-CSF) and granulocyte CSF (G-CSF), amongst other tumor-secreted growth factors [4], and likely activated by many different pro-inflammatory stimuli, such as interleukin 6 (IL-6), IL-1 $\beta$ , tumor necrosis factor (TNF) or interferon  $\gamma$  (IFN- $\gamma$ ) [5]. MDSCs are currently divided into two phenotypically and functionally different main subpopulations in mouse and three predominant populations in man: PMN-MDSCs are described as CD11b<sup>+</sup>Ly6C<sup>int</sup>Ly6G<sup>+</sup> and M-MDSCs as CD11b<sup>+</sup>Ly6C<sup>high</sup>Ly6G<sup>-</sup> in mouse while, in man, PMN-MDSCs are characterized as CD11b<sup>+</sup>CD14<sup>-</sup>CD33<sup>+</sup>CD66<sup>+</sup>HLA-DR<sup>-/low</sup> and M-MDSCs as CD11b<sup>+</sup>CD14<sup>+</sup>CD33<sup>+</sup>HLA-DR<sup>-/low</sup>. The third main population, described only in man, are lineage marker negative HLA-DR<sup>-</sup>CD33<sup>+</sup> early-stage MDSCs (eMDSCs) lacking the expression of CD14/CD15 [6]. Once actively recruited, MDSCs in the tumor microenvironment (TME) interfere with tumor rejection by dampening the host immune response against the tumor cells [5, 7]. Utilizing a plethora of different mechanisms, including the inhibition of T cell recruitment, the deprivation of nutrients compulsory for T cell proliferation in the TME or the secretion of immunosuppressive transforming growth factor  $\beta$  (TGF- $\beta$ ), MDSCs inhibit T cell and NK cell functions essential for cancer cell rejection. The MDSC-mediated recruitment of regulatory T cells further contributes to immunosuppression in the TME [5, 7]. Beside their involvement in tumor progression, MDSCs participate in the orchestration of pre-metastatic niche formation in secondary organs [8, 9].

However, still little is known about the dynamics of MDSC migration *in vivo*. Over the last years, non-invasive imaging techniques such as positron emission tomography (PET) have proven to be sensitive tools to quantitatively monitor cell migration and homing dynamics *in vivo* in different areas of research, using either indirect or direct cell labeling methods [10, 11]. Indirect cell labeling for PET imaging requires the introduction of an imaging reporter gene in the cell type of interest, such as the herpes simplex virus-1 thymidine kinase (HSV1-tk) with high substrate specificity to the radioactive tracers 2'-deoxy-2'-[<sup>18</sup>F]fluoro-5-ethyl-1- $\beta$ -D-arabino-furanosyl-uracil ([<sup>18</sup>F]FEAU) or 9-(4-[<sup>18</sup>F]fluoro-3-[hydroxymethyl]butyl)guanine ([<sup>18</sup>F]-FHBG) [12, 13].

Direct cell labeling can be readily performed *in vitro*, e.g. with lipophilic imaging probes or radiolabeled antibodies [10, 11]. Herein, the PET imaging time window is limited by radionuclide half-life time. Imaging time windows of up to 48 h are enabled by the use of the lipophilic PET probe [<sup>64</sup>Cu]pyruvaldehyde-bis(N4-methylthiosemicarbazone) ([<sup>64</sup>Cu]PTSM), for example in context of inflammatory disease [10] or regenerative medicine [14]. Radioactively labeled monoclonal antibodies (mAbs) or engineered antibody fragments are the most often used imaging reporters for the direct, *in situ* labeling and monitoring of endogenous immune cells in cancer [15-17].

As MDSCs expand *in vivo* from two different hematopoietic precursor cells and share cell surface markers with myeloid cells such as monocytes, macrophages and neutrophils, specific *in situ* labeling poses difficulties [18, 19]. In previous work, we have labeled murine PMN-MDSCs with the fluorescent dye formulation DiD to follow their migration in primary and metastatic PyMT breast cancer-bearing mice via optical imaging (OI) [20]. Due to the methodological limitations of tissue penetration and spatial resolution of OI, we have now chosen to adapt our recently established antibody-receptor targeting approach for PET imaging towards MDSCs. With this method, we could previously radiolabel murine CD4<sup>+</sup> T helper cells efficiently and reliably by targeting the T cell receptor with a radioactively labeled mAb [11]. In comparison to the unspecific, passive uptake of [<sup>64</sup>Cu]PTSM, active internalization of the receptor-antibody-complex provided higher stability of the radiolabel with simultaneously less detrimental effects on cell viability and function [11, 21]. We have now successfully transferred this approach to PMN- and M-MDSCs *in vitro* generated from bone marrow progenitor cells using CD11b (integrin  $\alpha_M$ ) as target for radiolabeling. As  $\alpha_M\beta_2$  heterodimer with the common integrin  $\beta_2$ , CD11b is implicated in adhesion of neutrophils and monocytes to activated endothelium as well as in phagocytosis by recognition of inactivated complement components [22]. Being expressed widely on both murine and human MDSC subpopulations, the cell surface-bound CD11b poses an excellent target for MDSC radiolabeling. Using a <sup>64</sup>Cu-modified CD11b-specific mAb tagged with 1,4,7-triazacyclononane-triacetic acid (NOTA) as chelator, we were able to radiolabel both MDSC subpopulations with little effect on cell viability and function to reveal the kinetic of specific homing to the primary and metastatic TME in different cancer types. Sequentially, we followed the migration and tumor homing of both [<sup>64</sup>Cu]NOTA- $\alpha$ CD11b-mAb-labeled PMN- and M-MDSCs ([<sup>64</sup>Cu]PMN- and

[<sup>64</sup>Cu]M-MDSCs, respectively) in mouse models of primary and metastatic PyMT breast cancer and B16F10 melanoma. Moreover, the use of the common cell surface marker CD11b for radiolabeling enables straightforward translation of this imaging approach to other CD11b<sup>+</sup> cells, such as neutrophils, monocytes and macrophages.

## Methods

### Mice

C57BL/6N mice were purchased from Charles River Laboratories (Sulzfeld, Germany), C57BL/6-Tg(TcraTcrb)1100Mjb/Crl (OT-1) mice were bred in the service facility for transgenic animals at the University Hospital Tübingen. Mice were maintained under specific pathogen free conditions in individual ventilated cages with standard rodent pellet food and water ad libitum. Female C57BL/6N mice between 8-12 weeks of age were used for all experiments. All animal procedures were conducted in accordance with German federal regulations on the use and care of experimental animals, and approved by the local authorities (Regierungspräsidium Tübingen).

### Cell lines

All cell culture supplies were obtained from Merck Millipore (Biochrom, Merck Millipore, Burlington, Massachusetts, United States). The generation and maintenance of PyMT and luciferase positive (luc)-PyMT mammary tumor cell lines were previously described [9, 23]. The B16F10-Luc2 melanoma cell line was purchased from Perkin Elmer (Waltham, Massachusetts, United States) and maintained in RPMI 1640 supplemented with 10 % heat-inactivated fetal calf serum (FCS). Anti-mouse  $\alpha$ CD11b-mAb-producing M1/70 hybridoma cells (American Type Culture Collection, ATCC, Manassas, Virginia, United States) were cultured in DMEM containing 10 % heat-inactivated FCS, 1 mM sodium pyruvate, 1 % MEM-amino acids, 10 mM HEPES buffer, 100 U/mL Penicillin/Streptomycin and 0.05 mM 2-mercaptoethanol (Sigma Aldrich, St. Louis, Missouri, United States) (complete DMEM medium). All cell lines were maintained at 37 °C and 7.5 % CO<sub>2</sub> in a humidified incubator.

### MDSC generation

The *in vitro* generation of bone marrow-derived MDSCs was adapted from Marigo *et al.* [24]. Briefly, bone marrow cells were isolated from femur and tibiae of female C57BL/6 mice and kept overnight on UV-irradiated or sterile petri dishes in 5 mL RPMI 1640 medium supplemented with 10 % heat-inactivated FCS, 1 mM sodium pyruvate, 1 %

MEM-amino acids, 10 mM HEPES buffer, 100 U/mL Penicillin/Streptomycin and 0.05 mM 2-mercaptoethanol (complete RPMI medium). On day 1 of culture, cells were transferred to suspension cell culture plates (Sarstedt, Nümbrecht, Germany) in 10 mL complete RPMI medium supplemented with 40 ng/mL GM-CSF and 40 ng/mL IL-6 (PeproTech, Hamburg, Germany). Fresh cytokines were added on day 3 and 5 of culture, medium was changed when necessary. On day 6, the expanded PMN-MDSCs and M-MDSCs were separated according to Ly6G and Gr-1 expression by magnetic cell sorting (Miltenyi Biosciences, Bergisch Gladbach, Germany) following the manufacturer's instructions and analyzed by flow cytometry after staining with V500- $\alpha$ CD45.2 (clone: 104, BD Biosciences, Franklin Lakes, New Jersey, United States), APC-eFluor780- $\alpha$ CD11b (clone: 1A8, eBioscience, Thermo Fisher Scientific, Waltham, Massachusetts, United States), APC- $\alpha$ Ly6C (clone: HK1.4, BioLegend, San Diego, California, United States) and PE- $\alpha$ Ly6G (clone: 1A8, BD Biosciences) antibodies.

### Primary tumor and metastasis models

Primary PyMT breast cancer tumors were induced by orthotopic injection of 5x10<sup>5</sup> PyMT cells in 25  $\mu$ L saline into the left 4<sup>th</sup> mammary fat pad. PyMT breast cancer metastases were induced by *intracardiac* (*i.c.*) injection of 2.5x10<sup>5</sup> luc-PyMT cells in 100  $\mu$ L saline. PyMT breast cancer primary tumors and PyMT metastases were allowed to grow for 21 days. B16F10 primary melanomas were induced by *intracutaneous* injection of 2.5x10<sup>5</sup> B16F10-Luc2 cells in 25  $\mu$ L saline, while metastases were induced by *i.c.* injection of 1x10<sup>5</sup> B16F10-Luc2 cells in 100  $\mu$ L saline. B16F10 primary melanoma and melanoma metastases were allowed to grow for 14 days. Tumor size was monitored using calipers while metastatic growth of melanomas was monitored by bioluminescence OI. All inoculation procedures were performed under 1.5 % isoflurane anesthesia (flow rate 0.8 L/min) and experimental animals received analgesics before the injections and until 3 days after the *i.c.* injection.

### CD11b mAb isolation, NOTA conjugation and radiolabeling

The rat anti-mouse  $\alpha$ CD11b mAb (isotype: IgG<sub>2b</sub>) was purified from the M1/70 hybridoma cell line (ATCC) culture supernatants via affinity chromatography using HiTrap protein G columns (GE Healthcare, Little Chalfont, United Kingdom) with 1 mL column volume according to the manufacturer's instructions. The mAb concentration was determined via UV/Vis spectroscopy using a NanoDrop1000 photometer (Thermo Fisher Scientific)

and adjusted to 8 mg/mL in PBS using 100 kDa Amicon Ultra-15 Centrifugal Filter Units (Merck Millipore). To eliminate trace metal contaminations, the mAb solution was incubated first with 5  $\mu$ L 0.5 M EDTA (pH 7) and then washed three times in 0.1 M HEPES buffer (pH 7.5) treated with 1.2 g of Chelex 100 (Sigma Aldrich). NOTA-*N*-hydroxysuccinimide ester (NOTA-NHS, Macrocyclics, Plano, Texas, United States) was dissolved in Rotipuran Ultrapure water (Carl Roth, Karlsruhe, Germany) at a concentration of 10 mg/mL, and the conjugation reaction between the mAb and the NOTA-NHS ester was performed in a 55-fold molar excess over night at 4 °C. The NOTA- $\alpha$ CD11b-mAb was washed 7 times in sterile Chelex-treated 0.25 M sodium acetate (pH 6) and concentrated to 2-6 mg/mL using 100 kDa Amicon Ultra-15 Centrifugal Filter Units (Merck Millipore).

$^{64}\text{Cu}$  was produced as previously described [11, 21] and buffered to pH 5-6 with 0.5 M ammonium acetate for antibody radiolabeling. The NOTA- $\alpha$ CD11b-mAb was incubated with [ $^{64}\text{Cu}$ ]CuCl<sub>2</sub> in a 2:1 ratio MBq: $\mu$ g protein for 60 min at 42 °C and the reaction was quenched with 1  $\mu$ L diethylenetriaminepentaacetic acid (20 mg/mL). Radiochemical purity was assessed by instant thin layer chromatography on silica gel with 0.1 M citrate (pH 5.0) as running buffer.

### Cell labeling using [ $^{64}\text{Cu}$ ]NOTA- $\alpha$ CD11b-mAb

Isolated PMN- and M-MDSCs were suspended at  $2 \times 10^6$  cells/mL in complete RPMI medium supplemented with 40 ng/mL GM-CSF and 40 ng/mL IL-6 (Peprotech). For radiolabeling,  $1 \times 10^6$  PMN- and M-MDSCs were dispensed into low adherence 48-well plates (Sarstedt). Subsequently, 0.74 MBq corresponding to 1.6  $\mu$ g [ $^{64}\text{Cu}$ ]NOTA- $\alpha$ CD11b-mAb in 20  $\mu$ L PBS were added to each well and incubated for 30 min at 37 °C. Cells were then washed twice and suspended in either PBS or complete medium, and the cell count was adjusted for adoptive transfer into tumor- or metastases-bearing mice or further *in vitro* investigation.

### [ $^{64}\text{Cu}$ ]NOTA- $\alpha$ CD11b-mAb uptake and efflux

The uptake of the [ $^{64}\text{Cu}$ ]NOTA- $\alpha$ CD11b-mAb into PMN- and M-MDSCs was determined by  $\gamma$ -counting (Perkin Elmer). Therefore,  $1 \times 10^5$  PMN- or M-MDSCs in 1 mL complete medium were transferred into  $\gamma$ -counting tubes directly after radiolabeling. The labeling stability and efflux of [ $^{64}\text{Cu}$ ]NOTA- $\alpha$ CD11b-mAb was determined directly, and 5, 24 and 48 h after initial radiolabeling by measuring radiolabeled [ $^{64}\text{Cu}$ ]PMN- and [ $^{64}\text{Cu}$ ]M-MDSCs and supernatants separately.

### Viability of [ $^{64}\text{Cu}$ ]NOTA- $\alpha$ CD11b-mAb-labeled MDSCs

To assess the effect of the [ $^{64}\text{Cu}$ ]NOTA- $\alpha$ CD11b-mAb labeling on the viability of PMN- and M-MDSCs, radiolabeled [ $^{64}\text{Cu}$ ]PMN- and [ $^{64}\text{Cu}$ ]M-MDSCs and unlabeled controls were stained with 7-aminoactinomycin D (7-AAD) and PE-Annexin V 3 and 48 h post radiolabeling using the PE Annexin V Apoptosis Detection Kit I (BD Biosciences). Staining was performed according to the manufacturer's instruction and samples were analyzed on a BD LSRFortessa flow cytometer (BD Biosciences). Data analysis was performed using the FlowJo software Version 10 (Tree Star, Inc., Ashland, Oregon, United States).

### Immunosuppression assay

The capacity of naïve *in vitro* expanded,  $\alpha$ CD11b-mAb-labeled PMN- and M-MDSCs (CD11b-PMN and CD11b-M-MDSCs, respectively) and [ $^{64}\text{Cu}$ ]PMN- and [ $^{64}\text{Cu}$ ]M-MDSCs to suppress T cell proliferation was evaluated in a carboxyfluorescein succinimidyl ester (CFSE)-dilution assay. MDSCs were labeled with  $\alpha$ CD11b-mAb or [ $^{64}\text{Cu}$ ]NOTA- $\alpha$ CD11b-mAb as described above. CD8<sup>+</sup> T cells were isolated from the spleen and extraperitoneal lymph nodes of C57BL/6-Tg(TcraTcrb)1100Mjb/Crl (OT-1) mice using a T cell isolation kit (Miltenyi Biosciences). Freshly isolated OT-1 CD8<sup>+</sup> T cells were stained with carboxyfluorescein diacetate succinimidyl ester at a final concentration of 1.25  $\mu$ M in PBS (Cell trace Kit, Life Technologies, Thermo Fisher Scientific) and T cell proliferation was stimulated with 50 U IL-2 (Novartis, Basel, Switzerland), 8  $\mu$ g/mL SIINFEKL peptide (EMC Microcollections, Tübingen, Germany) and the T Cell Activation and Expansion Kit (Miltenyi Biosciences) according to the manufacturer's instructions. CFSE-labeled OT-1 T cells and naïve *in vitro* expanded, CD11b-PMN- and CD11b-M-MDSCs or [ $^{64}\text{Cu}$ ]PMN- and [ $^{64}\text{Cu}$ ]M-MDSCs were incubated in different cell to cell ratios for 72 h in a 96-well plate. Flow cytometric analysis was performed on the BD LSRFortessa (BD Biosciences). The percentage of T cell proliferation for each condition was assessed according to CFSE-dilution in comparison to T cells alone using the FlowJo software (Tree Star).

### CD11b blocking

To assess the availability of CD11b binding sites on MDSCs after prelabeling with 1.6  $\mu$ g  $\alpha$ CD11b-mAb (clone M1/70), PMN- and M-MDSCs were stained for 30 min at 4 °C with Cy5-modified  $\alpha$ CD11b-mAb (clone M1/70) 3, 24 and 48 h post initial prelabeling. Unlabeled PMN- and M-MDSCs served as control.

Flow cytometric analysis was performed on a BD LSRII flow cytometer (BD Biosciences). Data was analyzed with FlowJo (TreeStar).

### Fluorescence microscopy

To visualize internalization of the anti-mouse Cy3- $\alpha$ CD11b-mAb, PMN- and M-MDSC were labeled with Cy3- $\alpha$ CD11b-mAb as described, cell samples were fixed in 2 % formalin, pipetted onto a microscopy slide and analyzed directly after preparation.

Staining for phosphorylated H2A.X histones as an indication for DNA-double strand breaks was performed after MDSC fixation in 2 % PBS-buffered formalin followed by two washing steps in Rotipuran Ultrapure water (Carl Roth) and 10 min heat-fixation onto microscopy slides. MDSC cell samples were permeabilized with 0.3 % Triton X-100 in 10 % donkey serum for 30 min. After washing, microscopy slides were incubated in anti-phosphorylated H2A.X antibody (1:200, Abcam) for 1 h, washed and stained with donkey anti-rabbit F(ab')<sub>2</sub>-Cy3 (1:500, Dianova) and donkey anti-rat F(ab')<sub>2</sub>-Alexa 488 (1:500, Dianova) for 1 h. Staining with DAPI (1:10000, Sigma Aldrich) was used for the visualization of cell nuclei.

For the *ex vivo* validation of MDSC migration to the primary PyMT- and B16F10 melanoma tumors, paraffin-embedded tumor tissue sections were deparaffinized, rehydrated, and incubated in citrate buffer pH 6.0 for 2 min in a pressure cooker for antigen recovery before cooling in deionized water for 10 min at room temperature. After washing, tumor tissue sections were blocked in donkey serum (1:20 dilution, 30 min) and incubated with rabbit anti-Ki-67 (1:100, Abcam, Cambridge, United Kingdom) for 1 h as a marker for proliferating tumor cells. Secondary antibody staining was performed for 1 h with anti-rabbit Alexa 647 (1:500, Dianova, Hamburg, Germany) and anti-rat-Cy3 (1:500, Dianova) to identify adoptively transferred MDSCs labeled with the rat  $\alpha$ CD11b-mAb. Then, cell nucleus staining with Yopro nuclear dye (Molecular Probes, Thermo Fisher Scientific) was performed. All images were acquired on the LSM 800 microscope (Zeiss, Oberkochen, Germany) operated under the Zen software (Version 2.3).

### Flow cytometric profiling for endogenous MDSCs

To assess the frequency of endogenous PMN- and M-MDSCs, PyMT breast cancer and B16F10 melanoma tumors were inoculated as described, isolated and cut into small pieces (approximately 1.5-2 mm in height and width). Tumor tissue was then digested with 2 mg/mL Collagenase Type IV (Sigma

Aldrich) in DMEM supplemented with 5 % FCS and 10 mM HEPES buffer for 40 min at 37 °C. Then, the tissue was washed first through a 70  $\mu$ m cell strainer, then through a 40  $\mu$ m cell strainer. Remaining erythrocytes were lysed with 3 mL ACK lysing buffer (Lonza, Basel, Switzerland) for 4 min at room temperature. The tumor cell suspension was then pipetted into a 5 mL polystyrene tube via a 40  $\mu$ m cell strainer snap cap (Corning, New York, United States), counted and 5x10<sup>6</sup> cells were used for antibody staining. Single cell suspensions were stained with BV510- $\alpha$ CD45 (clone: 30-F11), AF700- $\alpha$ B220 (clone: RA3-6B2), BV421- $\alpha$ Ly6C (clone: HK1.4), BV605- $\alpha$ CD11b (clone: M1/70), BV711- $\alpha$ Ly6G (clone: 1A8), BV785- $\alpha$ CD11c (clone: N418), FITC- $\alpha$ CD3 (clone: 500A2), PerCP- $\alpha$ CD4 (clone: RM4-5), BV650- $\alpha$ CD8a (clone: 53-6.7), PE/Cy7- $\alpha$ I-A/I-E (clone: M5/114.15.2) and PE- $\alpha$ F4/80 (clone: BM8) for 30 min at 4 °C, washed three times in PBS, fixed in 0.5 % formalin and analyzed on the BD LSRFortessa flow cytometer (BD Biosciences).

### G-CSF ELISA

Plasma levels of G-CSF in PyMT breast cancer- and B16F10 melanoma-bearing mice were determined with a standard ELISA (R&D Systems, Minneapolis, Minnesota, United States) according to the manufacturer's instructions. Therefore, retro-orbital blood was sampled from PyMT breast cancer- and B16F10 melanoma-bearing mice directly after CO<sub>2</sub> asphyxiation into an EDTA-containing micro tube (Sarstedt), cellular blood components were separated via centrifugation and the resulting plasma was stored at -80 °C until use.

### Bioluminescence OI

Bioluminescence OI measurements to monitor metastatic growth of PyMT breast cancer- or B16F10 melanoma-metastatic lesions were performed with the IVIS Spectrum OI system (Perkin Elmer) on shaved and depilated experimental animals. Experimental animals were anesthetized with 1.5 % isoflurane in oxygen, injected intraperitoneally with 200  $\mu$ L Luciferin (XenoLight, D-Luciferin - K<sup>+</sup> salt, Perkin Elmer) with a final dose of 150 mg/kg bodyweight and imaged 2 min after injection to allow Luciferin to distribute. Bioluminescence images were acquired with open emission filter, medium binning and f-stop 1 in a 14x14 cm FOV as images sequences with exposure times of 10, 30, 60 and 120 sec. *Ex vivo* bioluminescence images were acquired directly after organ isolation on non-reflective black paper with the same settings as described.

### In vivo imaging using PET/MR.

Tumor- or metastases-bearing experimental

animals and naïve littermate controls were anesthetized with 1.5 % isoflurane in oxygen with a flow rate of 0.8 L/min in a temperature-controlled anesthesia box. For the *intravenous (i.v.)* adoptive cell transfer, a catheter was inserted into the tail vein directly before injection of either  $2 \times 10^6$  [ $^{64}\text{Cu}$ ]PMN-MDSCs or [ $^{64}\text{Cu}$ ]M-MDSCs corresponding to approximately 0.028-0.037 MBq. Static 20 min emission PET scans were acquired 3, 24 and 48 h post adoptive cell transfer on a dedicated small-animal Inveon microPET scanner (Siemens Healthineers, Erlangen, Germany), followed by T2-weighted anatomical magnetic resonance (MR) scans using a TurboRARE protocol (TR = 1800 ms; TE = 90.51 ms; field of view 76.8x34.8x22.8 mm<sup>3</sup>, image size 256x116x76) with a rat whole-body volume coil (inner diameter: 86 mm) on the 7 T BioSpec 70/30 MR scanner (Bruker, Ettlingen, Germany).

### PET image reconstruction, data analysis and statistics

PET images were reconstructed as previously described [11] in Inveon Acquisition Workplace 1.5.0.28 (Siemens Healthineers). Briefly, static histogram files were constructed from list-mode data and images were reconstructed by applying an ordered subset expectation maximization algorithm in two dimensions (Fourier rebinning, OSEM2D, 16 subsets, 4 iterations, pixel size 128x128, matrix 0.79x0.79 mm<sup>2</sup>). Attenuation correction was not performed. PET images were corrected for radioactive decay, normalized to the amount of injected activity and fused with the anatomical MR images with the help of glass capillaries containing [ $^{64}\text{Cu}$ ]NOTA- $\alpha$ CD11b-mAb solution in Inveon Research Workplace (Siemens Healthineers). Volumes of interest (VOI) were drawn on the lung, liver and spleen on the anatomical MR image, cell uptake in primary tumors and metastases was quantified by drawing VOIs on hot spots on the PET images co-registered to the MR images for anatomical guidance. The percentage of injected dose per cubic centimeter (%ID/cm<sup>3</sup>) values were calculated as follows: mean activity in VOI/(injected activity\*10<sup>6</sup>)/100.

### Ex vivo biodistribution analysis

To validate the *in vivo* PET data, the biodistribution of [ $^{64}\text{Cu}$ ]PMN-MDSCs and [ $^{64}\text{Cu}$ ]M-MDSCs was analyzed by  $\gamma$ -counting *ex vivo* after the 48 h imaging time point. Retro-orbital blood was sampled directly after the animal was sacrificed by CO<sub>2</sub> asphyxiation. For the primary tumor models, the tumor, lungs, liver, spleen, kidneys, the left femur and tibia and muscle tissue were harvested for

biodistribution analysis.

For the metastasis models, tissue margins between healthy and cancerous tissue were determined by *ex vivo* bioluminescence OI and the cancerous tissue was separated from the healthy organ as far as technically possible. In this way, metastases were separated from the heart, lungs, liver, spleen, kidneys, adrenal glands, ovaries, femur and tibiae and subjected to  $\gamma$ -counting separately from the healthy tissue.

A standard solution with a known amount of radioactivity served as reference to calculate the percentage of injected dose per gram of tissue (%ID/g). The tubes containing the standard solution and the organs were measured in the Wizard2 automated  $\gamma$ -counter (Perkin Elmer) at an energy window of 350 to 650 keV. The resulting decay corrected counts per minute were then first normalized to the injected dose with the help of the standard solution and to the respective weight of the organ to obtain %ID/g.

### Statistics

Comparative %ID/cm<sup>3</sup> values of experimental groups are given as mean  $\pm$  SEM. For statistical analysis, two-tailed Student's t-test or Dunnett's Multiple Comparison Test were applied. Resulting p-values <0.05 were considered significant (\*).

## Results

### Characterization of bone marrow-derived MDSCs

In tumor-bearing hosts, MDSC expand from progenitors in the bone marrow under the influence of growth factors and pro-inflammatory cytokines. Hence, PMN- and M-MDSCs used for cell tracking studies were expanded from bone marrow-derived progenitor cells with GM-CSF and IL-6 according to a previously published protocol [24]. The resulting cells were magnetically separated and subsequently subjected to flow cytometric and morphologic characterization. The assessed phenotypes were characteristic for PMN-MDSCs and M-MDSCs, respectively (Figure 1A). PMN-MDSCs were characterized as CD11b<sup>+</sup>Ly6C<sup>+</sup>Ly6G<sup>+</sup> with a ring-shaped nucleus (Figure 1B, left panel) while M-MDSCs were characterized as CD11b<sup>+</sup>Ly6C<sup>+</sup>Ly6G<sup>-</sup> with a round nucleus (Figure 1B, right panel).

### Labeling of PMN- and M-MDSCs with a Cy5-conjugated CD11b-specific mAb and target internalization

The integrin CD11b was selected as target for radiolabeling of MDSCs. Being involved in adhesion and endocytotic processes of complement-bound

proteins, fast internalization and re-expression of CD11b were assumed [25]. To assess the amount of accessible CD11b-binding sites, we conjugated the fluorescent dye Cy5 to the CD11b-specific mAb and stained both PMN- and M-MDSC with Cy5- $\alpha$ CD11b-mAb at 3, 24 and 48 h after initial 30 min prelabeling with 1.6  $\mu$ g  $\alpha$ CD11b-mAb (Figure 2). CD11b-prelabeling reduced the available binding sites on both PMN- and M-MDSCs at 3 h ( $48.63 \pm 2.16$  % vs.  $63.40 \pm 1.28$  %,  $**p < 0.01$  for PMN- and  $37.67 \pm 2.65$  % vs.  $51.43 \pm 1.74$  %,  $**p < 0.01$  for M-MDSCs, respectively), while CD11b re-expression was completed at 24 h post labeling ( $79.13 \pm 2.44$  % vs.  $79.90 \pm 4.64$  % for PMN-MDSCs and  $71.67 \pm 0.42$  % vs.  $61.80 \pm 1.78$  %,  $**p < 0.01$  for M-MDSCs). Comparable to 24 h post prelabeling, there was no significant reduction in CD11b expression in pre-labeled MDSC samples compared to unlabeled controls ( $97.97 \pm 0.09$  % vs.  $97.13 \pm 0.41$  % for PMN-MDSCs and  $96.73 \pm 0.24$  % vs.  $93.93 \pm 1.00$  % for M-MDSCs) at 48 h (Figure 2A-B). The internalization of the mAb into PMN- and M-MDSCs was verified by confocal microscopy of a Cy3-modified CD11b-specific mAb directly depicting the internalization of the Cy3- $\alpha$ CD11b-mAb-integrin complex as early as 3 h post Cy3- $\alpha$ CD11b-mAb labeling of the cells (Figure 2C-D).

#### **In vitro evaluation of MDSC labeling with a $^{64}\text{Cu}$ -radiolabeled NOTA-modified CD11b-mAb**

According to our previously published evaluation on the amount of radioactivity dosage for murine CD4<sup>+</sup> T cell labeling [11], PMN- and M-MDSCs were radiolabeled with 0.74 MBq [ $^{64}\text{Cu}$ ]NOTA- $\alpha$ CD11b-mAb/ $10^6$  cells (corresponding to 1.6  $\mu$ g mAb) for 30 min at 37 °C. This approach resulted in a high stability of radioactivity on both [ $^{64}\text{Cu}$ ]PMN- and [ $^{64}\text{Cu}$ ]M-MDSCs at 5 h post radiolabeling ( $86.17 \pm 0.03$  % of initially measured radioactivity for [ $^{64}\text{Cu}$ ]PMN-MDSCs and  $84.12 \pm 0.02$  % of initially measured radioactivity for [ $^{64}\text{Cu}$ ]M-MDSCs, Figure 3A) while at 24 h post radiolabeling, approximately 50 % of initially applied radioactivity was detectable in both MDSC subpopulations ( $53.23 \pm 0.01$  % for [ $^{64}\text{Cu}$ ]PMN-MDSCs and  $51.81 \pm 0.02$  % for [ $^{64}\text{Cu}$ ]M-MDSCs). Intracellular radioactivity was further decreased at 48 h post initial radiolabeling ( $37.89 \pm 0.01$  % of initially measured radioactivity for [ $^{64}\text{Cu}$ ]PMN-MDSCs and  $35.43 \pm 0.02$  % of initially measured radioactivity for [ $^{64}\text{Cu}$ ]M-MDSCs) (Figure 3A). Beside positron emission,  $^{64}\text{Cu}$  decays via electron capture resulting in the generation of high-energy Auger electrons that can elicit DNA damage when in close proximity to the nucleus [26].

DNA damage can impair cell functionality, reduce cell viability and lead to the induction of apoptosis. Therefore, we evaluated the effect of cell labeling with 0.74 MBq [ $^{64}\text{Cu}$ ]NOTA- $\alpha$ CD11b-mAb on cell viability and apoptosis induction in PMN- and M-MDSCs. A non-significant decrease of viability of [ $^{64}\text{Cu}$ ]PMN-MDSCs ( $74.74 \pm 0.50$  % vs.  $79.43 \pm 1.78$  % viable control PMN-MDSCs) and [ $^{64}\text{Cu}$ ]M-MDSCs ( $86.06 \pm 0.63$  % vs.  $86.10 \pm 0.17$  % viable control M-MDSCs) was detected by 7-AAD staining at 3 h post radiolabeling (Figure 3B).

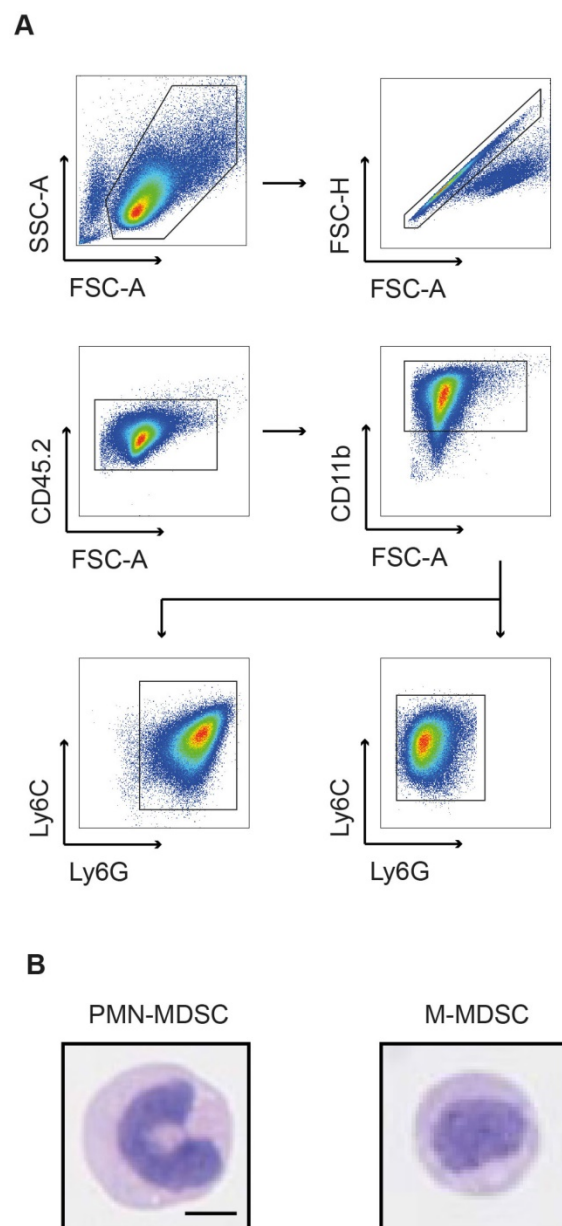


**Figure 1: Flow cytometric and morphologic characterization of bone marrow-derived MDSCs. (A)** Flow cytometric analysis of bone-marrow derived MDSCs characterized PMN-MDSCs as CD11b<sup>+</sup>Ly6C<sup>+</sup>Ly6G<sup>+</sup> and M-MDSCs as CD11b<sup>+</sup>Ly6C<sup>+</sup>Ly6G<sup>-</sup>. **(B)** Exemplary H&E staining of bone marrow-derived MDSCs confirmed the characteristic nuclear morphology of PMN-MDSCs (ring-like, left panel) and M-MDSCs (round, right panel). Scale bar 5  $\mu$ m.

Viability of both [ $^{64}\text{Cu}$ ]PMN-MDSCs ( $65.27 \pm 0.50\%$  vs.  $63.00 \pm 1.19\%$  viable control PMN-MDSCs) and [ $^{64}\text{Cu}$ ]M-MDSCs ( $70.70 \pm 0.31\%$  vs.  $65.53 \pm 3.08\%$  viable control M-MDSCs) decreased further over the 48 h examination period, however, no significant effect of the radiolabel was detected (Figure 3B). The fraction of phosphatidylserine-exposing [ $^{64}\text{Cu}$ ]PMN-MDSCs ( $20.17 \pm 0.77\%$  vs.  $13.70 \pm 1.53\%$  of unlabeled control PMN-MDSCs) and [ $^{64}\text{Cu}$ ]M-MDSCs ( $12.20 \pm 0.40\%$  vs.  $7.31 \pm 0.10\%$  of unlabeled control M-MDSCs) increased significantly at 3 h post radiolabeling in comparison to untreated controls as detected by PE-Annexin V staining (Figure 3C). At 48 h post radiolabeling, a further increase in Annexin V-positive [ $^{64}\text{Cu}$ ]M-MDSCs ( $13.57 \pm 0.75\%$  vs.  $17.23 \pm 1.77\%$  of unlabeled controls) and [ $^{64}\text{Cu}$ ]PMN-MDSCs ( $19.50 \pm 0.85\%$  vs.  $17.23 \pm 1.37\%$  of unlabeled controls) could be detected while, however, no significant effect of the [ $^{64}\text{Cu}$ ]NOTA- $\alpha\text{CD11b}$ -mAb labeling was detected (Figure 3C). Since their immunosuppressive feature is

considered a key function defining MDSCs, cell functionality after [ $^{64}\text{Cu}$ ]NOTA- $\alpha\text{CD11b}$ -mAb labeling was measured as capacity to suppress antigen-induced T cell proliferation. Antibody labeling with  $\alpha\text{CD11b}$ -mAb had no statistically significant effect on the immunosuppressive capacity of PMN-MDSCs or M-MDSCs compared to unlabeled controls (Figure 3D and E, respectively). Likewise, labeling with [ $^{64}\text{Cu}$ ]NOTA- $\alpha\text{CD11b}$ -mAb did not have any significant effect on the suppressive activity of PMN- and M-MDSCs (Figure 3D and E, respectively). The phosphorylation of H2A.X family histones was assessed as an early sign for DNA damage by immunofluorescence staining. Although  $^{64}\text{Cu}$  internalization into the cells led to radiation-induced DNA double strand breaks only at 48 h post radiolabeling in both [ $^{64}\text{Cu}$ ]PMN- and [ $^{64}\text{Cu}$ ]M-MDSCs (Figure 3F), cell functionality was not overtly affected (Figure 3D-E), suggesting that this cell labeling approach was feasible for *in vivo* cell migration studies.

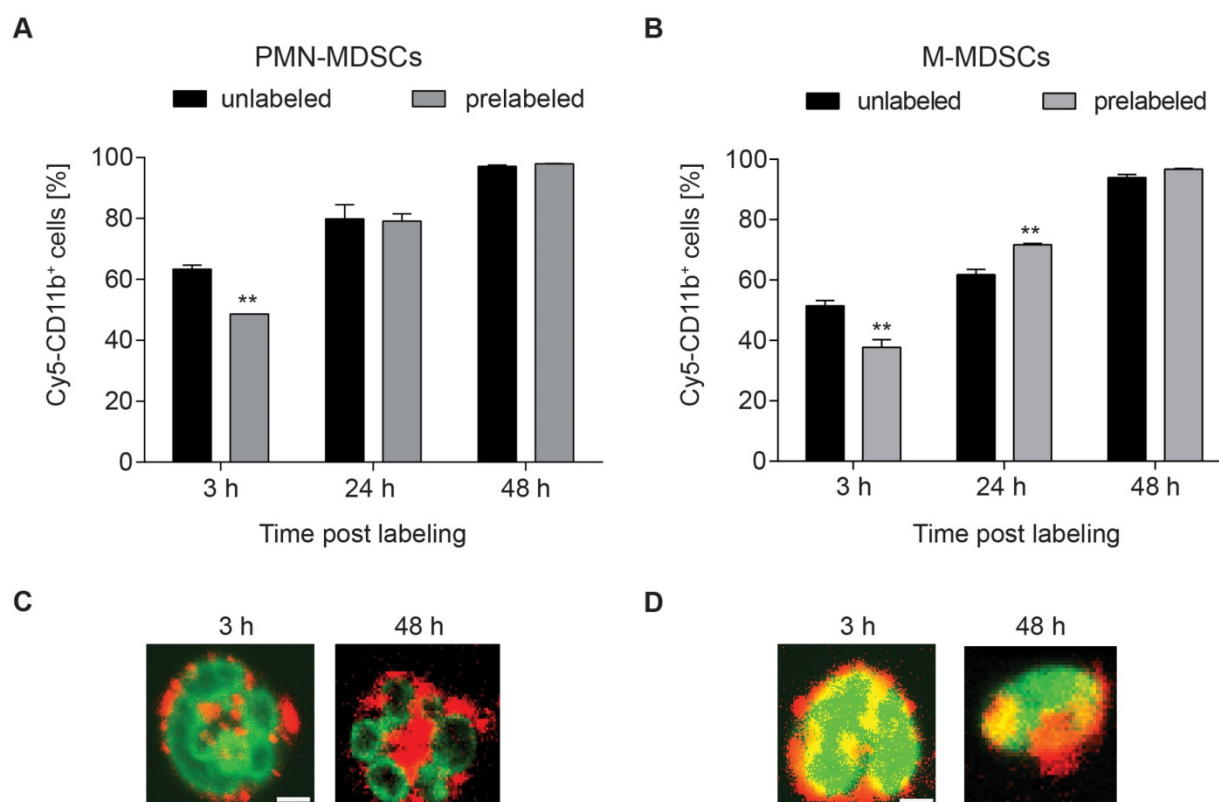


**Figure 2: Internalization of the  $\alpha\text{CD11b}$ -mAb-CD11b complex and CD11b re-expression.** Flow cytometric quantification of CD11b expression by Cy5- $\alpha\text{CD11b}$  staining of PMN-MDSCs (**A**) and M-MDSCs (**B**) 3, 24 and 48 h after prelabeling with  $1.6\ \mu\text{g}$   $\alpha\text{CD11b}$ -mAb revealed a reduced CD11b availability at 3 h post prelabeling and CD11b re-expression after 24 h. Confocal microscopy of PMN- (**C**) and M-MDSCs (**D**) 3 h and 48 h after labeling with  $1.6\ \mu\text{g}$  Cy3- $\alpha\text{CD11b}$  proved internalization of the CD11b-antibody complex within 3 h and retention in the cells over 48 h. Green – YoPro, red – Cy3- $\alpha\text{CD11b}$ , scale bar:  $1\ \mu\text{m}$ . All values are given as mean percent of total cells  $\pm$  SEM, n=3, statistics: Student's t-test with \*\*p<0.01.

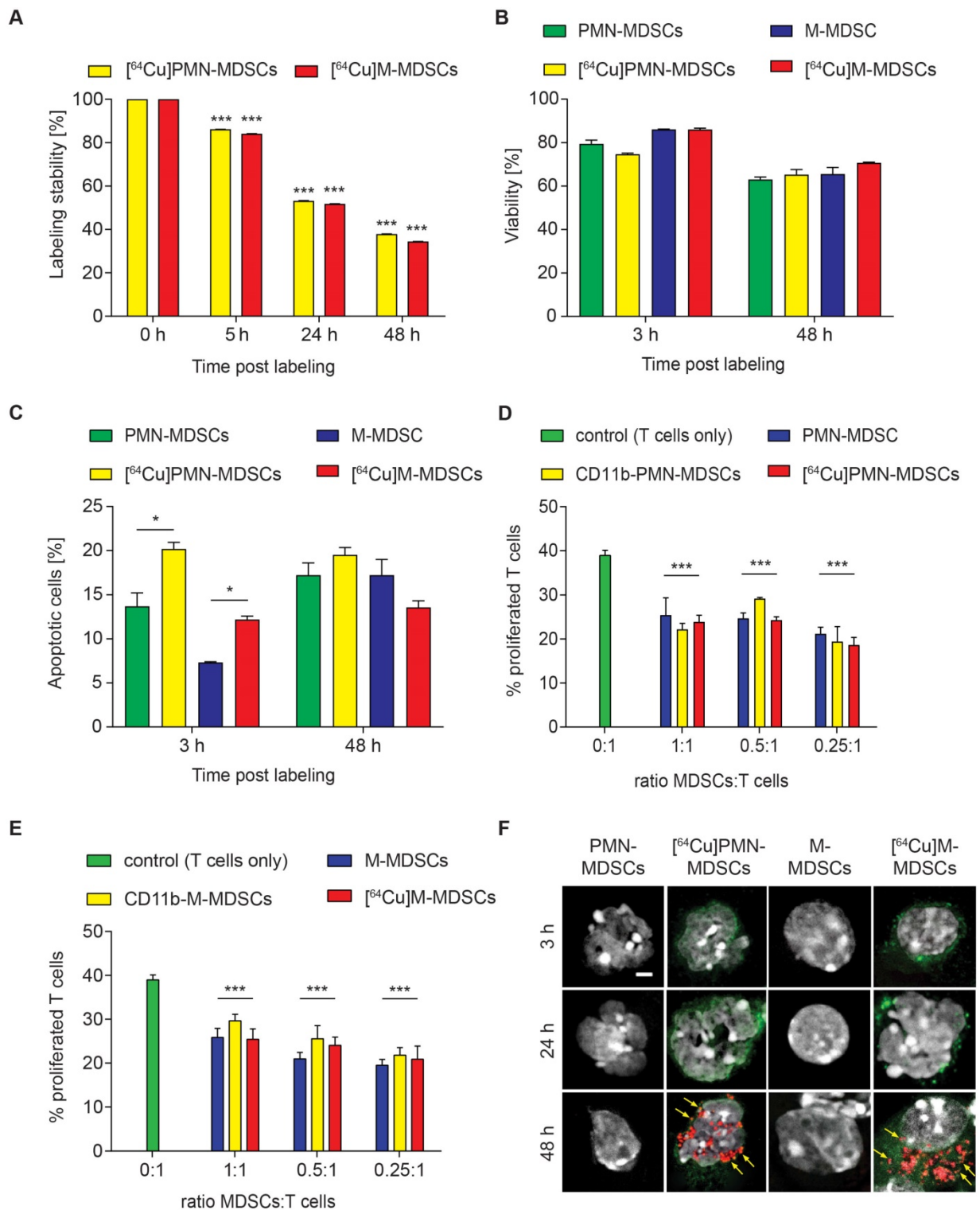


**Figure 3: Evaluation of [<sup>64</sup>Cu]NOTA-αCD11b-mAb labeling effects on PMN- and M-MDSCs. (A)** *In vitro* evaluation of [<sup>64</sup>Cu]NOTA-αCD11b-mAb labeling stability on PMN-MDSCs and M-MDSCs 5, 24 and 48 h after radiolabeling measured by γ-counting reveals only mediocre stability of the radiolabel at 48 h after radiolabeling. Data is normalized to the 0 h time point measured directly after radiolabeling as initial activity in PMN- and M-MDSCs, respectively (mean ± SEM in percent, n=9, statistics: Dunnett's Multiple Comparison Test, \*\*\*p<0.001). Flow cytometric analysis of viability (B) and apoptosis induction (C) of PMN- and M-MDSCs after labeling with the [<sup>64</sup>Cu]NOTA-αCD11b-mAb revealed reduced viability and significantly enhanced apoptosis induction in [<sup>64</sup>Cu]PMN- and [<sup>64</sup>Cu]M-MDSCs at 3 h after radiolabeling compared to unlabeled controls (mean ± SEM in percent, n=3) while the effect of radiolabeling was not as pronounced at 48 h after radiolabeling. Immunosuppression assay with *in vitro* expanded naïve PMN-(D)/M-MDSCs (E), CD11b-PMN-/M-MDSCs and [<sup>64</sup>Cu]PMN- and [<sup>64</sup>Cu]M-MDSCs demonstrated no significant loss in functionality as measured by capacity to inhibit antigen-induced proliferation of CFSE-labeled OT-I CD8<sup>+</sup> T cells after radiolabeling (mean ± SEM in percent, n=4, statistics: Dunnett's Multiple Comparison Test, \*\*\*p<0.001). Representative images of immunofluorescence staining for phosphorylated H2A.X histones as early markers for DNA damage (F) at 3, 24 and 48 h after radiolabeling with [<sup>64</sup>Cu]NOTA-αCD11b-mAb revealed DNA damage only at 48 h post radiolabeling in [<sup>64</sup>Cu]PMN- and [<sup>64</sup>Cu]M-MDSCs while no signs for DNA damage could be detected in unlabeled controls. Red – phosphorylated H2A.X, green – αCD11b mAb, white – DAPI nuclear dye, scale bar: 2 μm. Yellow arrows indicate sites of phosphorylated H2A.X histones.

## Tumor homing of [<sup>64</sup>Cu]PMN- and [<sup>64</sup>Cu]M-MDSCs to primary breast cancer and melanoma

To visualize *in vivo* MDSC migration by PET imaging,  $2 \times 10^6$  [<sup>64</sup>Cu]PMN- or [<sup>64</sup>Cu]M-MDSCs were injected *i.v.* into PyMT breast tumor- or B16F10 melanoma-bearing mice directly after radiolabeling. Static PET scans and T2-weighted anatomical MR scans were acquired 3, 24 and 48 h after MDSC transfer. As cell migration is relatively slow compared to metabolic processes, significant fractions of [<sup>64</sup>Cu]PMN- and [<sup>64</sup>Cu]M-MDSCs were detected in PyMT breast or B16F10 melanoma tumors only at 24 h after adoptive cell transfer. At 24 h after adoptive cell transfer, a significantly higher fraction of [<sup>64</sup>Cu]PMN-MDSCs could be located in B16F10 melanomas compared to PyMT breast tumors ( $3.66 \pm 0.34$  %ID/cm<sup>3</sup> vs  $1.67 \pm 0.23$  %ID/cm<sup>3</sup>, \*\**p*<0.01) (Figure 4A). Moreover, more [<sup>64</sup>Cu]M-MDSCs migrated into B16F10 melanomas than into PyMT breast tumors ( $3.14 \pm 0.15$  %ID/cm<sup>3</sup> vs  $1.74 \pm 0.29$  %ID/cm<sup>3</sup>, \*\**p*<0.01, Figure 4B). At 48 h post adoptive cell transfer, PET imaging showed a significantly higher uptake of [<sup>64</sup>Cu]PMN-MDSCs in B16F10 melanomas than in PyMT breast tumors ( $5.65 \pm 0.49$  %ID/cm<sup>3</sup> vs  $2.21 \pm 0.30$  %ID/cm<sup>3</sup>, \*\**p*<0.01, Figure 4A). No significant difference in the recruitment of [<sup>64</sup>Cu]M-MDSCs to both tumor types was detected 48 h post injection (Figure 4B). Compared to [<sup>64</sup>Cu]PMN-MDSCs, a higher fraction of [<sup>64</sup>Cu]M-MDSCs migrated to the PyMT breast tumors 48 h post *i.v.* injection. Interestingly, more [<sup>64</sup>Cu]PMN-MDSCs tended to migrate to B16F10 melanomas compared to [<sup>64</sup>Cu]M-MDSCs at both 24 and 48 h post injection. The differences in the uptake of MDSC subpopulations into PyMT breast cancer tumors and B16F10 melanoma indicate specific MDSC recruitment mechanisms to different tumor types. Furthermore, at all examined time points, the PET signal derived from [<sup>64</sup>Cu]PMN-MDSCs and [<sup>64</sup>Cu]M-MDSCs in both cancer types was not homogeneously distributed throughout the whole tumor but rather constituted hot spot areas (Figure 4A-B). The lungs, liver and spleen of primary PyMT breast cancer- and B16F10 melanoma-bearing mice represented further sites of [<sup>64</sup>Cu]PMN-MDSCs (Figure S1) and [<sup>64</sup>Cu]M-MDSCs (Figure S2) recruitment.

To correlate the uptake of adoptively transferred [<sup>64</sup>Cu]PMN- and [<sup>64</sup>Cu]M-MDSCs to endogenous MDSCs in the examined tumor models, PyMT breast cancer and B16F10 melanoma tumors were further examined for the frequency of endogenous PMN- (Figure 4C) and M-MDSCs (Figure 4D) by flow

cytometry according to the expression of CD11b, Ly6C and Ly6G. Therefore, single cell suspensions were prepared from PyMT breast cancer and B16F10 melanoma tumors, stained and analyzed for CD11b, Ly6C and Ly6G expressing cell populations. Interestingly, B16F10 melanoma tumors showed significantly higher levels of both endogenous PMN- ( $0.65 \pm 0.17$  % vs.  $0.17 \pm 0.06$  %, \**p*<0.05) and M-MDSCs ( $5.30 \pm 0.93$  % vs.  $1.30 \pm 0.36$  %, \*\**p*<0.01) than PyMT tumors. However, the frequency of M-MDSCs (Figure 4D) was considerably higher in both PyMT breast and B16F10 melanoma tumors. As M-MDSCs were identified as CD11b<sup>+</sup>Ly6C<sup>+</sup>Ly6G<sup>-</sup> cells, however, a clear and unambiguous discrimination of M-MDSCs and other tumor-resident myeloid cells was not possible.

## Recruitment of [<sup>64</sup>Cu]PMN- and [<sup>64</sup>Cu]M-MDSCs to lung metastatic lesions

Recent theories describe metastasis as a multi-step process including preceding pre-metastatic niche formation accompanied by immune evasion in secondary organs [8]. The microenvironment of established metastases should therefore differ from the primary TME and, in conclusion, recruitment dynamics of MDSCs to metastases might differ from primary tumor homing. To examine a possible difference in MDSC migration kinetics to the primary and metastatic microenvironments, PyMT breast cancer and B16F10 melanoma metastases were induced by *i.c.* injection of tumor cells into the left ventricle. Metastases-bearing mice received an adoptive transfer of  $2 \times 10^6$  [<sup>64</sup>Cu]PMN- or [<sup>64</sup>Cu]M-MDSCs via *i.v.* injection and PET and MR images were acquired 3, 24 and 48 h post MDSC transfer. Bioluminescence OI images were acquired at 48 h post adoptive transfer.

At 24 h post adoptive transfer, MDSC recruitment to B16F10 melanoma lung metastatic lesions was significantly higher in comparison to PyMT breast cancer lung metastatic lesions for both [<sup>64</sup>Cu]PMN- ( $8.21 \pm 1.02$  %ID/cm<sup>3</sup> vs  $4.16 \pm 0.79$  %ID/cm<sup>3</sup>, \**p*<0.05, Figure 5A and C) and [<sup>64</sup>Cu]M-MDSCs ( $8.61 \pm 1.80$  %ID/cm<sup>3</sup> vs  $5.13 \pm 1.71$  %ID/cm<sup>3</sup>, Figure 5D and F). [<sup>64</sup>Cu]PMN-MDSC uptake further increased at 48 h post transfer, with significantly higher cell fractions in B16F10 melanoma metastatic lesions compared to PyMT breast cancer metastatic lesions ( $10.10 \pm 1.60$  %ID/cm<sup>3</sup> vs  $5.01 \pm 0.85$  %ID/cm<sup>3</sup>, \**p*<0.05, Figure 5A and C). A slight but not significant increase of [<sup>64</sup>Cu]M-MDSC uptake was found in both cancer metastatic lesions at 48 h post transfer (Figure 5D and F). Representative bioluminescence images of the PyMT breast cancer and B16F10 melanoma metastases-bearing animals

are given in Figure 5B and E. At all examined time points, recruitment of both  $[^{64}\text{Cu}]\text{PMN-}$  and  $[^{64}\text{Cu}]\text{M-MDSCs}$  to B16F10 melanoma lung metastatic lesions was enhanced compared to PyMT breast cancer metastatic lesions. Furthermore, in comparison to the primary tumors, both metastatic lesions showed enhanced recruitment of both  $[^{64}\text{Cu}]\text{PMN}$  and

$[^{64}\text{Cu}]\text{M-MDSCs}$ , indicating differences in the capacity to recruit immunosuppressive MDSC to the respective microenvironment. Other sites of  $[^{64}\text{Cu}]\text{PMN-MDSC}$  and  $[^{64}\text{Cu}]\text{M-MDSC}$  recruitment in both metastasis models included the liver and spleen (Figure S3 and S4, respectively).

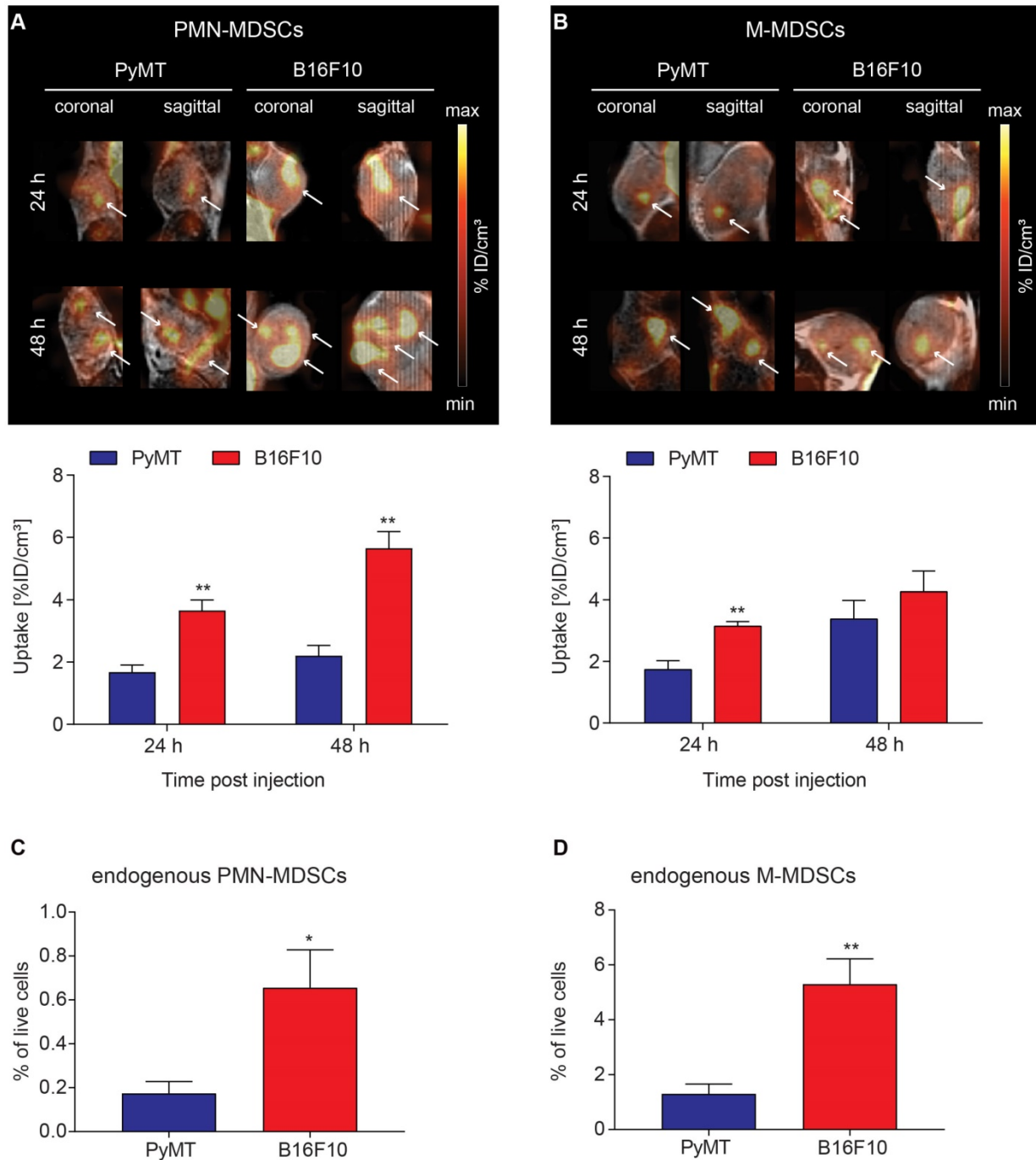


**Figure 4: Visualization of  $[^{64}\text{Cu}]\text{PMN-MDSC}$  and  $[^{64}\text{Cu}]\text{M-MDSC}$  homing to primary tumors and correlation with endogenous MDSCs.** Representative coronal and sagittal PET/MR images of (A)  $[^{64}\text{Cu}]\text{PMN-MDSCs}$  and (B)  $[^{64}\text{Cu}]\text{M-MDSCs}$  in primary PyMT breast tumors (left panel) and primary B16F10 melanoma (right panel). White arrows highlight hot spots of  $[^{64}\text{Cu}]\text{PMN-}$  and  $[^{64}\text{Cu}]\text{M-MDSC}$  uptake in the tumors revealing non-homogeneous cell distribution. Quantification of  $[^{64}\text{Cu}]\text{PMN-MDSC}$  (A, lower panel) and  $[^{64}\text{Cu}]\text{M-MDSC}$  (B, lower panel) migration 24 h and 48 h post injection (mean  $\pm$  SEM in %ID/cm<sup>3</sup>,  $[^{64}\text{Cu}]\text{PMN-MDSC}$ : n=5 for PyMT, n=6 for B16F10 and  $[^{64}\text{Cu}]\text{M-MDSC}$ : n=6 for PyMT, n=5 for B16F10, statistics: Student's t-test, \*\*p<0.01) revealed increased  $[^{64}\text{Cu}]\text{PMN-}$  and  $[^{64}\text{Cu}]\text{M-MDSC}$  homing to B16F10 melanomas in comparison to PyMT tumors. Correlation of uptake values of adoptively transferred  $[^{64}\text{Cu}]\text{PMN-}$  and  $[^{64}\text{Cu}]\text{M-MDSCs}$  to the endogenous PMN- (C) and M-MDSCs (D) in the PyMT and B16F10 tumors revealed a similar pattern of MDSCs in the tumors with higher cell frequencies of PMN- and M-MDSCs in the primary B16F10 tumors than the PyMT tumors (n=4, statistics: two-tailed Student's t-test, \*p<0.05, \*\*p<0.01).

### Ex vivo validation

To confirm *in vivo* tumor homing of [ $^{64}\text{Cu}$ ]PMN- and [ $^{64}\text{Cu}$ ]M-MDSCs, experimental animals were sacrificed, primary PyMT breast tumors excised and prepared for histological staining. Due to the ambiguity of the cell surface markers for murine MDSCs, we aimed to identify adoptively transferred

MDSCs by means of their antibody label for PET imaging. By staining for the rat anti-mouse  $\alpha\text{CD11b-mAb}$ , we could validate data gathered from *in vivo* cell tracking experiments: PMN- (Figure 6A) and M-MDSCs (Figure 6B) could be identified in relative close proximity to blood vessels in the cancer mass.

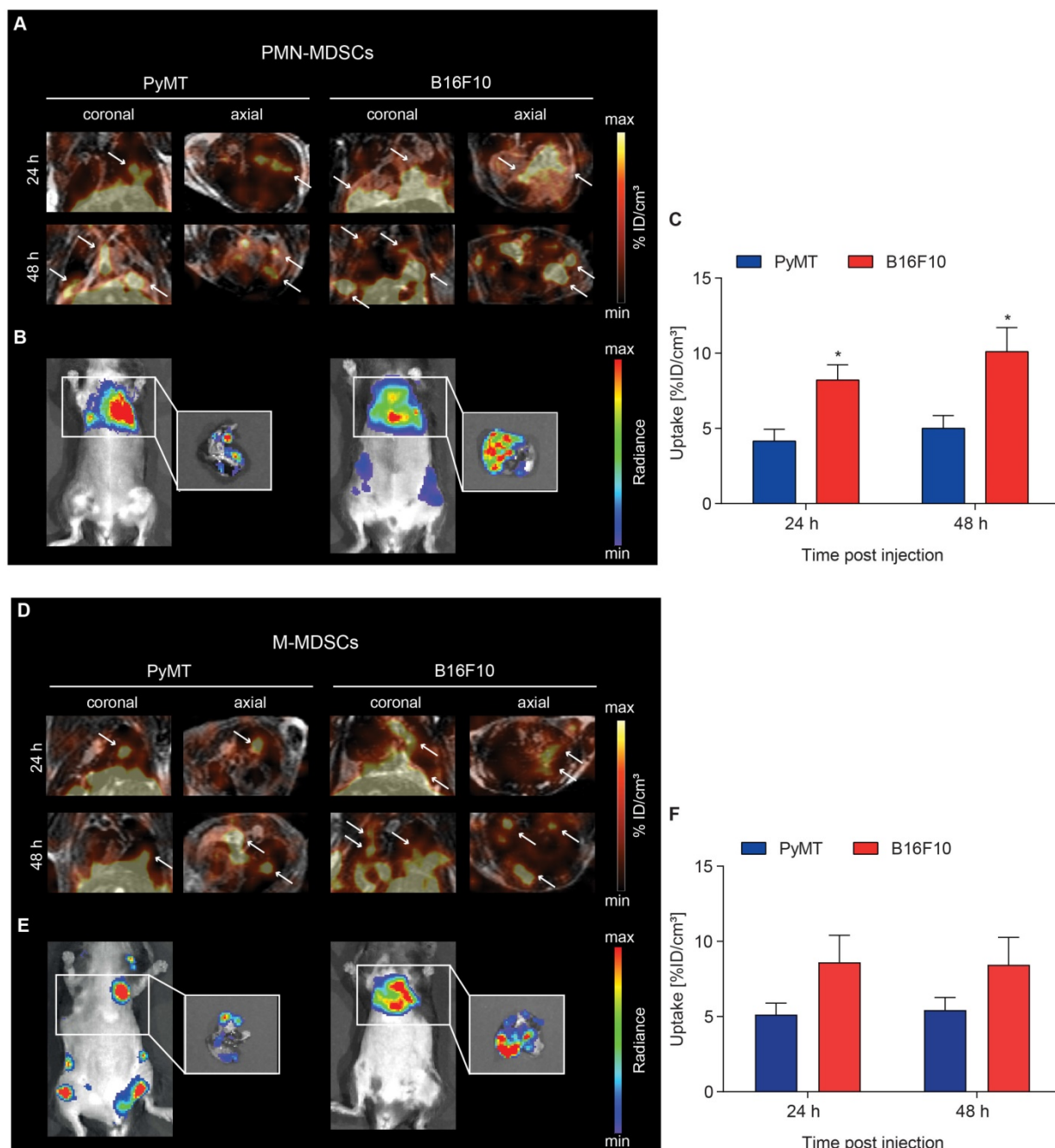


**Figure 5: Visualization of [ $^{64}\text{Cu}$ ]PMN- and [ $^{64}\text{Cu}$ ]M-MDSC homing to lung metastatic PyMT breast cancer and B16F10 melanoma.** Representative coronal and axial PET/MR images of [ $^{64}\text{Cu}$ ]PMN-MDSCs (upper panel, **A**) and [ $^{64}\text{Cu}$ ]M-MDSC (lower panel, **D**) in PyMT breast cancer lung metastatic lesions (left panel) and B16F10 melanoma lung metastatic lesions (right panel). White arrows highlight hot spots of [ $^{64}\text{Cu}$ ]PMN-MDSCs and [ $^{64}\text{Cu}$ ]M-MDSCs in the metastatic lungs. *In vivo* whole-body and *ex vivo* (white boxes, zoom on the isolated lungs after sacrifice) bioluminescence OI images of the metastases-bearing mice (**B** and **E**, respectively) were acquired 48 h post adoptive cell transfer. Quantification of cell migration 24 h and 48 h post injection demonstrates enhanced [ $^{64}\text{Cu}$ ]PMN-MDSC (**C**) and [ $^{64}\text{Cu}$ ]M-MDSC (**F**) homing to the B16F10 melanoma metastatic microenvironment as compared to PyMT breast cancer metastatic microenvironment (mean  $\pm$  SEM in %ID/cm<sup>3</sup>, [ $^{64}\text{Cu}$ ]PMN-MDSC: n=7 for PyMT, n=6 for B16F10 and [ $^{64}\text{Cu}$ ]M-MDSC: n=6 for PyMT, n=5 for B16F10, statistics: two-tailed Student's t-test, \* p<0.05).

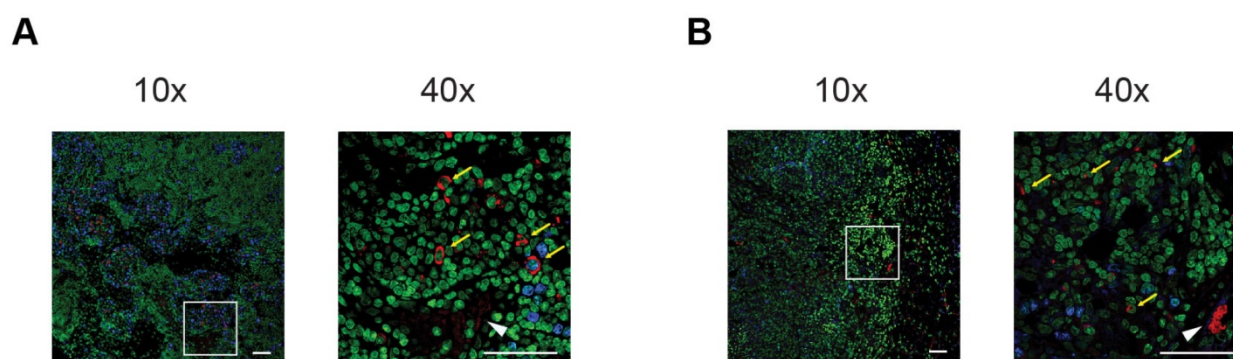


**Figure 6: Immunofluorescence staining confirms the *in vivo* cell trafficking data.** Representative immunofluorescence stainings of PyMT breast cancer tumors after adoptive transfer of [ $^{64}\text{Cu}$ ]PMN-MDSCs (A) or [ $^{64}\text{Cu}$ ]M-MDSCs (B), respectively, confirm that the *in vivo* signal detected as hot spot areas in PET imaging in the PyMT breast tumors is derived from adoptively transferred [ $^{64}\text{Cu}$ ]PMN- or [ $^{64}\text{Cu}$ ]M-MDSCs. Accordingly, both [ $^{64}\text{Cu}$ ]PMN- and [ $^{64}\text{Cu}$ ]M-MDSCs are not distributed homogeneously throughout the tumor sample but localize in close proximity to blood vessels. Yellow arrows indicate adoptively transferred MDSCs, white arrow head indicated blood vessel. Blue - Ki-67, green - Yopro nuclear dye, red -  $\alpha\text{CD11b}$  mAb, scale bar 50  $\mu\text{m}$ .

## Discussion and Conclusions

By suppression of both innate and adaptive immune responses, MDSCs are key players, not only in tumor progression but also in pre-metastatic niche formation and metastasis [5, 7]. In cancer patients, high percentages of MDSCs in peripheral blood are generally associated with poor prognosis [27-29]. Although MDSCs are under close investigation, *in vivo* migration of MDSCs has not yet been studied extensively with non-invasive imaging. In previous work, we were able to visualize migration of *in vitro* generated, DiD-labeled PMN-MDSCs to primary PyMT breast tumors with fluorescence OI [20]. In a similar study, Combes *et al.* followed the migration of MDSCs labeled with DiR, a dye closely related to DiD, in BALB/c mice bearing syngeneic 4T1 breast tumors with fluorescence OI. Herein, the authors compared *in vitro* generated MDSCs and MDSCs isolated from the bone marrow of tumor-bearing mice, however, subpopulations were not separated before adoptive transfer [30]. In the second MDSC tracking study published so far, Gr1<sup>+</sup> MDSCs isolated from the spleen of cervical cancer-bearing mice were labeled with superparamagnetic iron oxide particles (SPIOs) for MR imaging in subcutaneous cervical cancer-bearing mice. Adoptively transferred MDSCs were detected as signal hypointensity in the tumors [31]. The detection of hypointense regions, however, constitutes a major drawback of cell tracking with SPIOs as necrotic or cystic areas in tumors might be detected as hypointense signals as well.

We here present, to our knowledge, the first MDSC tracking study employing PET as quantitative non-invasive imaging modality. We have successfully applied our previously established cell labeling protocol [11, 21] on MDSCs by use of the [ $^{64}\text{Cu}$ ]NOTA- $\alpha\text{CD11b}$ -mAb to label MDSCs *in vitro*. Radiolabeling of the MDSCs *in vitro* did not result in

an unreasonably high cell loss during labeling or compromise viability of the cells. Apoptosis induction, however, was more severe in [ $^{64}\text{Cu}$ ]PMN-MDSCs compared to [ $^{64}\text{Cu}$ ]M-MDSCs at both assessed time points post initial radiolabeling. Interestingly, M-MDSCs seem to express higher levels of cell death inhibiting molecules and proteins [32], which might explain the observed differences in the fraction of apoptotic cells after radiolabeling. Internalization of the mAb-integrin-complex for intracellular labeling was faster than expected from previous studies and completed within 3 h. This might be due to the different signaling and membrane shuttling kinetics of T cell receptors and integrins. Furthermore, the mAb-integrin-complex should only be approximately half the size of the previously examined mAb-TCR-complex, which might affect the efficiency and speed of the internalization. Interestingly, overall CD11b expression increased over 48 h in both prelabeled and control MDSC samples presumably due to stimulation mediated by the cytokine supplements in the growth medium. Enhanced CD11b cell surface expression by translocation of preformed CD11b to the cell membrane was reported in neutrophils upon activation or stimulation [33, 34]. Radiation, especially the decay of  $^{64}\text{Cu}$  via the emission of highly energetic Auger electrons, might induce DNA double strand breaks. Although a small fraction of both [ $^{64}\text{Cu}$ ]PMN- and [ $^{64}\text{Cu}$ ]M-MDSCs did stain positive for phosphorylated H2A.X as early sign for DNA damage at 48 h post initial radiolabeling, we did not expect pronounced effects on cell behavior during the following experiments as the observation period for cell tracking with  $^{64}\text{Cu}$  was set to 48 h only. MDSC cell functionality after radiolabeling was measured as suppressive activity against antigen-induced T cell proliferation. While the capacity to inhibit T cell proliferation was not significantly reduced in

[<sup>64</sup>Cu]PMN- and [<sup>64</sup>Cu]M-MDSCs in comparison to unlabeled control MDSCs, a characteristic reduction of T cell proliferation with increasing numbers of MDSCs was not observed. Additionally, the percentage of proliferated T cells was low in the T cell only control even under stimulation with the T cell-cognate antigen. As the interplay between activated T cells and MDSCs has recently been described as pivotal for MDSC suppressive function [35], we concluded that due to the low activation state of the T cells no difference between the examined conditions could be observed. Furthermore, the stability of the radiolabel was assessed in both [<sup>64</sup>Cu]PMN- and [<sup>64</sup>Cu]M-MDSCs. Although the efflux of radioactivity from [<sup>64</sup>Cu]PMN- and [<sup>64</sup>Cu]M-MDSCs was higher than expected from previously examined murine T cells [11], the stability of the antibody-based radiolabeling was still superior to [<sup>64</sup>Cu]PTSM in murine T cells [11] and presumably other compounds usually used for cell labeling such as 2-deoxy-2-[<sup>18</sup>F]fluoroglucose [36], [<sup>111</sup>In]Oxine or [<sup>99m</sup>Tc]HMPAO [37]. This discrepancy, however, emphasizes the importance of the *in vitro* evaluation of the mAb used for receptor targeting of the specific cell type of interest.

As common myeloid cell marker, CD11b can serve as a target for radiolabeling different kinds of myeloid cells including monocytes, macrophages or neutrophils. Therefore, further translation of this indirect radiolabeling approach to other cell types of interest is straightforward and achievable. So far, macrophages [38-40] have only been tracked *in vivo* by MR imaging. The hypointense or negative contrast of the MR imaging labeling agent, however, might be difficult to interpret in certain tissues, for example in the lung, or certain tissue conditions such as necrosis. Additionally, the presented labeling approach permits labeling and imaging of cell populations that cannot be targeted specifically *in situ* with radiolabeled antibodies or antibody fragments such as MDSCs. However, it comes with certain drawbacks: direct labeling approaches, such as the antibody-receptor targeting approach described, do not permit monitoring of cell viability or functionality *in vivo*. Furthermore, direct labeling approaches might suffer from label, and hence, signal dilution over time when not terminally differentiated, proliferating cells are labeled. Repetitive imaging is restricted to the biological half-life of the label. Nevertheless, direct labeling approaches are commonly more readily applicable to different cell types of interest than indirect labeling approaches. Indirect labeling approaches rely on genetic modifications, e.g. the introduction of a reporter gene suitable for the imaging modality of choice, of cell types or whole

organisms which can be time- and labor-intensive [13, 41, 42]. Therefore, our combined PET and MR imaging approach could provide a valuable platform for the imaging of CD11b<sup>+</sup> cell subsets with high detection sensitivity and spatial resolution.

As discussed above, the direct labeling approach applied to visualize [<sup>64</sup>Cu]PMN- and [<sup>64</sup>Cu]M-MDSC trafficking *in vivo* does not permit interrogation of the cells' state after adoptive transfer into the tumor-bearing hosts. In a previous study, however, we were able to non-invasively image the migration of bone marrow-derived MDSCs to the primary PyMT breast cancer TME. In a subsequent analysis, the fluorescent dye used for fluorescence OI permitted the assessment of the fate of the adoptively transferred MDSCs: the isolated cells were viable or differentiated further into dendritic cells or macrophages. While both viable and further differentiated cells could be detected, fractions of the adoptively transferred MDSCs might have been phagocytosed by e.g. macrophages [20]. And while it would be highly interesting to examine if the functional capacity of the adoptively transferred MDSCs was changed *in vivo*, it would be challenging to specifically isolate the transferred cells as their phenotype is similar to endogenous MDSCs and functional assessment *ex vivo* with an immunosuppression assay would need high numbers of pure cells.

In the last decade, the frequency of MDSCs in the peripheral blood of tumor-bearing mice or cancer patients was heavily examined and further correlated with disease stage and survival [27, 43, 44]. In this study, the experimental separation of the *in vitro* generated MDSCs allowed us to temporally quantify tumor and metastases homing and examine tumor tropism of the subpopulations PMN- and M-MDSCs. In the primary tumor models, the PyMT breast tumors tended to recruit a higher proportion of adoptively transferred [<sup>64</sup>Cu]M-MDSCs while B16F10 primary melanomas were more profoundly infiltrated by [<sup>64</sup>Cu]PMN-MDSCs. Comparably, Toh *et al.* reported PMN-MDSCs as the predominant MDSC subpopulation in the tumors of a transgenic murine melanoma model and further indicated PMN-MDSC-mediated promotion of cancer cell dissemination in this model [45].

Beside the stronger recruitment to the primary tumors, [<sup>64</sup>Cu]PMN-MDSCs showed an increased signal in the *ex vivo* biodistribution analysis of various organs including the blood of the B16F10 melanoma-bearing animals at 48 h post MDSC transfer. This observation prompted the question if survival of [<sup>64</sup>Cu]PMN-MDSCs in tumor-bearing mice was enhanced in comparison to [<sup>64</sup>Cu]M-MDSCs. As

G-CSF is an important growth factor promoting steady-state myelopoiesis and, in particular, the production and differentiation of neutrophils [46], the G-CSF plasma levels in PyMT breast tumor- and B16F10 melanoma-bearing mice were analyzed. Interestingly, plasma levels of G-CSF did not differ significantly between PyMT breast cancer- and B16F10 melanoma-bearing mice (Figure S5) indicating that primary B16F10 melanoma tumors recruited higher fractions of [ $^{64}\text{Cu}$ ]PMN-MDSCs independently of cell survival.

To further correlate the uptake of adoptively transferred [ $^{64}\text{Cu}$ ]PMN-MDSCs and [ $^{64}\text{Cu}$ ]M-MDSCs to endogenous MDSCs in the PyMT breast tumors and B16F10 melanoma tumors, flow cytometric profiling of the immune cell infiltrates in these tumors was performed. Interestingly, while B16F10 melanomas showed higher frequencies of both endogenous PMN- and M-MDSCs than PyMT breast tumors, the distribution of the MDSC subpopulations, however, did not correlate exactly with the uptake values of adoptively transferred MDSCs. Adoptively transferred MDSCs were characterized by cell surface marker expression for their phenotypes and an immunosuppression assay for their functionality according to current recommendations before transfer into tumor-bearing mice [6]. Profiling for endogenous PMN-MDSCs as CD11b<sup>+</sup>Ly6C<sup>int</sup>Ly6G<sup>+</sup> cells and endogenous M-MDSCs as CD11b<sup>+</sup>Ly6C<sup>+</sup>Ly6G<sup>-</sup> cells, however, did not allow for a clear functional discrimination according to current recommendations. As other tumor-resident myeloid cells such as tumor-associated macrophages, are also characterized as CD11b<sup>+</sup>Ly6C<sup>+</sup>Ly6G<sup>-</sup>, we assumed that, in parallel with endogenous M-MDSCs, we further detected a substantial frequency of heterogeneous tumor-associated macrophages [47].

Independent of the MDSC subpopulation, MDSCs fundamentally affect many different stages of tumor invasion and metastasis by, e.g., modulation of the extracellular matrix at the invasive margins and tumor vascularization as well as promotion of metastatic outgrowth [48, 49]. Correspondingly, in the examined metastasis models, overall MDSC recruitment was considerably higher than in the corresponding primary tumor models. Additionally, B16F10 melanoma lung metastases recruited a higher fraction of the adoptively transferred [ $^{64}\text{Cu}$ ]PMN-MDSCs and [ $^{64}\text{Cu}$ ]M-MDSCs than PyMT breast cancer lung metastases.

Moreover, B16F10 primary melanomas and melanoma metastases in the lungs exhibited higher uptake of both [ $^{64}\text{Cu}$ ]PMN- and [ $^{64}\text{Cu}$ ]M-MDSCs in comparison to primary and metastatic PyMT breast cancer. The difference in the recruitment of

radiolabeled MDSC subpopulations to the primary and metastatic TME of these cancer types reflects current literature on MDSC subpopulations in cancer patients: The more aggressively growing B16F10 melanoma model recruited more radiolabeled MDSCs independently of the subpopulation reflecting, to some extent, poor prognosis and overall survival in patients with high frequency of MDSCs in peripheral blood. Interestingly, current literature reports both an increase in the frequency of M-MDSCs in the peripheral blood of patients with malignant melanoma and an overall increase of PMN- and M-MDSCs in melanoma patients [50, 51]. Immune checkpoint inhibitor treatment was further correlated with an early decrease in the frequency of peripheral blood PMN-MDSCs in a small melanoma patient cohort [52].

Due to their immunosuppressive nature, MDSCs receive considerable attention as possible negative players in cancer immunotherapeutic approaches [53, 54]. While strategies to deplete, to further differentiate MDSCs or to modulate MDSC function in the TME have been published [55-57], newly emerging studies report combinations of MDSC-targeting agents with more and more routinely used immunotherapy approaches [58-60]. Clinical *in situ* imaging of MDSC migration in cancer patients with, e.g. immunoPET, however, is challenging due to the lack of an MDSC-specific marker that can be targeted with an immunoPET tracer. Therefore, our molecular imaging approach to visualize MDSC migration and tumor homing *in vivo* could be used to further dissect the effects of combinational therapies and immunotherapeutics on MDSC migration and their capacity to infiltrate tumors or secondary tissues.

## Abbreviations

%ID/cm<sup>3</sup>: percentage of injected dose per cubic centimeter; %ID/g: percentage of injected dose per gram; [ $^{18}\text{F}$ ]FEAU: 2'-deoxy-2'-[ $^{18}\text{F}$ ]fluoro-5-ethyl-1- $\beta$ -D-arabinofuranosyl-uracil; [ $^{18}\text{F}$ ]FHBG: 9-(4-[ $^{18}\text{F}$ ]fluoro-3-[hydroxymethyl]butyl)guanidine; [ $^{64}\text{Cu}$ ]M-MDSCs: [ $^{64}\text{Cu}$ ]NOTA- $\alpha$ CD11b-mAb-labeled M-MDSCs; [ $^{64}\text{Cu}$ ]PMN-MDSCs: [ $^{64}\text{Cu}$ ]NOTA- $\alpha$ CD11b-mAb-labeled PMN-MDSCs; [ $^{64}\text{Cu}$ ]PTSM: [ $^{64}\text{Cu}$ ]pyruvaldehyde bis(N4-methylthiosemicarbazone); 7-AAD: 7-aminoactinomycin D; ATCC: American type culture collection; CD11b-M-MDSCs:  $\alpha$ CD11b-mAb labeled M-MDSCs; CD11b-PMN-MDSCs:  $\alpha$ CD11b-mAb labeled PMN-MDSCs; CFSE: carboxyfluorescein succinimidyl ester; eMDSCs: early-stage MDSCs; FCS: fetal calf serum; G-CSF: granulocyte colony stimulation factor; GM-CSF: granulocyte-macrophage colony stimulation factor; HSV1-tk: herpes simplex virus-1 thymidine kinase;

i.c.: intracardiac; IFN- $\gamma$ : interferon  $\gamma$ ; IL-6: interleukin 6; i.v.: intravenous; Luc: Luciferase; mAb: monoclonal antibody; M-CSF: macrophage colony stimulation factor; MDSCs: myeloid-derived suppressor cells; M-MDSC: monocytic myeloid-derived suppressor cells; MRI: magnetic resonance imaging; NOTA: 1,4,7-triazacyclononane-triacetic acid; NOTA-NHS: NOTA-N-hydroxysuccinimide ester; OI: optical imaging; PBS: phosphate buffered saline; PET: positron emission tomography; PMN-MDSCs: polymorphonuclear myeloid-derived suppressor cells; PyMT: polyoma middle T antigen; SPIOs: superparamagnetic iron oxide particles; TGF- $\beta$ : transforming growth factor  $\beta$ ; TME: the tumor microenvironment; TNF: tumor necrosis factor; VOI: volume of interest.

## Acknowledgements

The authors would like to thank Marie-Aline Neveu for valuable research input. We are grateful to Sandro Aidone, Maren Harant, Dennis Haupt, Natalie Mucha and Linda Schramm for excellent technical support. This work was founded by the Deutsche Forschungsgemeinschaft (DFG, German Research Foundation) under Germany's Excellence Strategy – EXC 2180 – 390900677, by the Research Fellowship of the German Research Foundation (GR4017/1-1) for CMG, the Fortüne Junior grant (2309-0-0) of the Medical Faculty for CMG, a research grant of the Henriette und Othmar Eier Stiftung for CMG and the Swiss Werner Siemens Foundation for BJP.

## Supplementary Material

Supplementary figures and tables.

<http://www.thno.org/v09p5869s1.pdf>

## Competing Interests

The authors have declared that no competing interest exists.

## References

1. Fidler IJ. The pathogenesis of cancer metastasis: the "seed and soil" hypothesis revisited. *Nat Rev Cancer*. 2003; 3: 453-8.
2. Seyfried TN, Huysentruyt LC. On the origin of cancer metastasis. *Crit Rev Oncog*. 2013; 18: 43-73.
3. Torre LA, Siegel RL, Ward EM, Jemal A. Global Cancer Incidence and Mortality Rates and Trends--An Update. *Cancer Epidemiol Biomarkers Prev*. 2016; 25: 16-27.
4. Bayne LJ, Beatty GL, Jhala N, Clark CE, Rhim AD, Stanger BZ, et al. Tumor-derived granulocyte-macrophage colony-stimulating factor regulates myeloid inflammation and T cell immunity in pancreatic cancer. *Cancer cell*. 2012; 21: 822-35.
5. Marvel D, Gabrilovich DI. Myeloid-derived suppressor cells in the tumor microenvironment: expect the unexpected. *J Clin Invest*. 2015; 125: 3356-64.
6. Bronte V, Brandau S, Chen S-H, Colombo MP, Frey AB, Greten TF, et al. Recommendations for myeloid-derived suppressor cell nomenclature and characterization standards. *Nat Commun*. 2016; 7: 12150.
7. Kumar V, Patel S, Tcyganov E, Gabrilovich DI. The Nature of Myeloid-Derived Suppressor Cells in the Tumor Microenvironment. *Trends Immunol*. 2016; 37: 208-20.
8. Sceneay J, Smyth MJ, Möller A. The pre-metastatic niche: finding common ground. *Cancer Metastasis Rev*. 2013; 32: 449-64.

9. Sceneay J, Chow MT, Chen A, Halse HM, Wong CSF, Andrews DM, et al. Primary Tumor Hypoxia Recruits CD11b<sup>+</sup>/Ly6C<sup>med</sup>/Ly6G<sup>+</sup> Immune Suppressor Cells and Compromises NK Cell Cytotoxicity in the Premetastatic Niche. *Cancer Res*. 2012; 72: 3906-11.
10. Griessinger CM, Kehlbach R, Bukala D, Wiehr S, Bantleon R, Cay F, et al. *In vivo* tracking of Th1 cells by PET reveals quantitative and temporal distribution and specific homing in lymphatic tissue. *J Nucl Med*. 2014; 55: 301-7.
11. Griessinger CM, Maurer A, Kesenheimer C, Kehlbach R, Reischl G, Ehrlichmann W, et al. <sup>64</sup>Cu antibody-targeting of the T-cell receptor and subsequent internalization enables *in vivo* tracking of lymphocytes by PET. *Proc Natl Acad Sci U S A*. 2015; 112: 1161-6.
12. Najjar AM, Nishii R, Maxwell DS, Volgin A, Mukhopadhyay U, Bornmann WG, et al. Molecular-genetic PET imaging using an HSV1-tk mutant reporter gene with enhanced specificity to acycloguanosine nucleoside analogs. *J Nucl Med*. 2009; 50: 409-16.
13. Thunemann M, Schorg BF, Feil S, Lin Y, Voelkl J, Golla M, et al. Cre/lox-assisted non-invasive *in vivo* tracking of specific cell populations by positron emission tomography. *Nat Commun*. 2017; 8: 444.
14. Huang J, Lee CC, Sutcliffe JL, Cherry SR, Tarantal AF. Radiolabeling rhesus monkey CD34<sup>+</sup> hematopoietic and mesenchymal stem cells with <sup>64</sup>Cu-pyruvaldehyde-bis(N4-methylthiosemicarbazone) for microPET imaging. *Mol Imaging*. 2008; 7: 1-11.
15. Tavare R, Escuin-Ordinas H, Mok S, McCracken MN, Zettlitz KA, Salazar FB, et al. An Effective Immuno-PET Imaging Method to Monitor CD8-Dependent Responses to Immunotherapy. *Cancer Res*. 2016; 76: 73-82.
16. Tavare R, McCracken MN, Zettlitz KA, Knowles SM, Salazar FB, Olafsen T, et al. Engineered antibody fragments for immuno-PET imaging of endogenous CD8<sup>+</sup> T cells *in vivo*. *Proc Natl Acad Sci U S A*. 2014; 111: 1108-13.
17. Rashidian M, Ingram JR, Dougan M, Dongre A, Whang KA, LeGall C, et al. Predicting the response to CTLA-4 blockade by longitudinal noninvasive monitoring of CD8 T cells. *J Exp Med*. 2017; 214: 2243-55.
18. Knowles SM, Wu AM. Advances in immuno-positron emission tomography: antibodies for molecular imaging in oncology. *J Clin Oncol*. 2012; 30: 3884-92.
19. Wu AM. Engineered antibodies for molecular imaging of cancer. *Methods*. 2014; 65: 139-47.
20. Sceneay J, Griessinger CM, Hoffmann SHL, Wen SW, Wong CSF, Krumeich S, et al. Tracking the fate of adoptively transferred myeloid-derived suppressor cells in the primary breast tumor microenvironment. *PLoS One*. 2018; 13: e0196040.
21. Hoffmann SHL, Maurer A, Reck DI, Reischl G, Pichler BJ, Kneilling M, et al. Murine Lymphocyte Labeling by <sup>64</sup>Cu-Antibody Receptor Targeting for *In Vivo* Cell Trafficking by PET/CT. *J Vis Exp*. 2017.
22. Solovjov DA, Pluskota E, Plow EF. Distinct roles for the alpha and beta subunits in the functions of integrin alphaMbeta2. *J Biol Chem*. 2005; 280: 1336-45.
23. Wong CSF, Sceneay J, House CM, Halse HM, Liu MCP, George J, et al. Vascular Normalization by Loss of Siah2 Results in Increased Chemotherapeutic Efficacy. *Cancer Res*. 2012; 72: 1694-704.
24. Marigo I, Bosio E, Solito S, Mesa C, Fernandez A, Dolcetti L, et al. Tumor-Induced Tolerance and Immune Suppression Depend on the C/EBP $\beta$  Transcription Factor. *Immunity*. 2010; 32: 790-802.
25. Mobberley-Schuman PS, Weiss AA. Influence of CR3 (CD11b/CD18) expression on phagocytosis of Bordetella pertussis by human neutrophils. *Infect Immun*. 2005; 73: 7317-23.
26. McMillan DD, Maeda J, Bell JJ, Genet MD, Phooswadi G, Mann KA, et al. Validation of <sup>64</sup>Cu-ATSM damaging DNA via high-LET Auger electron emission. *J Radiat Res*. 2015; 56: 784-91.
27. Diaz-Montero CM, Salem ML, Nishimura MI, Garrett-Mayer E, Cole DJ, Montero AJ. Increased circulating myeloid-derived suppressor cells correlate with clinical cancer stage, metastatic tumor burden, and doxorubicin-cyclophosphamide chemotherapy. *Cancer Immunol Immunother*. 2009; 58: 49-59.
28. Yu J, Du W, Yan F, Wang Y, Li H, Cao S, et al. Myeloid-derived suppressor cells suppress antitumor immune responses through IDO expression and correlate with lymph node metastasis in patients with breast cancer. *J Immunol*. 2013; 190: 3783-97.
29. Arihara F, Mizukoshi E, Kitahara M, Takata Y, Arai K, Yamashita T, et al. Increase in CD14<sup>+</sup>HLA-DR<sup>-low</sup> myeloid-derived suppressor cells in hepatocellular carcinoma patients and its impact on prognosis. *Cancer Immunol Immunother*. 2013; 62: 1421-30.
30. Combes F, Mc Cafferty S, Meyer E, Sanders NN. Off-Target and Tumor-Specific Accumulation of Monocytes, Macrophages and Myeloid-Derived Suppressor Cells after Systemic Injection. *Neoplasia*. 2018; 20: 848-56.
31. Tremblay ML, Davis C, Bowen CV, Stanley O, Parsons C, Weir G, et al. Using MRI cell tracking to monitor immune cell recruitment in response to a peptide-based cancer vaccine. *Magn Reson Med*. 2018; 80: 304-16.
32. Haverkamp JM, Smith AM, Weinlich R, Dillon CP, Qualls JE, Neale G, et al. Myeloid-derived suppressor activity is mediated by monocytic lineages maintained by continuous inhibition of extrinsic and intrinsic death pathways. *Immunity*. 2014; 41: 947-59.
33. Edwards SW. Cell signalling by integrins and immunoglobulin receptors in primed neutrophils. *Trends Biochem Sci*. 1995; 20: 362-7.

34. Zhou H, Liao J, Aloor J, Nie H, Wilson BC, Fessler MB, et al. CD11b/CD18 (Mac-1) is a novel surface receptor for extracellular double-stranded RNA to mediate cellular inflammatory responses. *J Immunol.* 2013; 190: 115-25.
35. Pinton L, Solito S, Damuzzo V, Francescato S, Pozzuoli A, Berizzi A, et al. Activated T cells sustain myeloid-derived suppressor cell-mediated immune suppression. *Oncotarget.* 2016; 7: 1168-84.
36. Rini JN, Bhargava KK, Tronco GG, Singer C, Caprioli R, Marwin SE, et al. PET with FDG-labeled Leukocytes versus Scintigraphy with <sup>111</sup>In-Oxine-labeled Leukocytes for Detection of Infection. *Radiology.* 2006; 238: 978-87.
37. Kelbaek H, Linde J, Nielsen SL. Evaluation of a new leukocyte labeling procedure with <sup>99m</sup>Tc-HMPAO. *Eur J Nucl Med.* 1988; 14: 621-3.
38. Bierry G, Jehl F, Boehm N, Robert P, Prevost G, Dietemann JL, et al. Macrophage activity in infected areas of an experimental vertebral osteomyelitis model: USPIO-enhanced MR imaging-feasibility study. *Radiology.* 2008; 248: 114-23.
39. Lefevre S, Ruimy D, Jehl F, Neuville A, Robert P, Sordet C, et al. Septic arthritis: monitoring with USPIO-enhanced macrophage MR imaging. *Radiology.* 2011; 258: 722-8.
40. Weissleder R, Nahrendorf M, Pittet MJ. Imaging macrophages with nanoparticles. *Nat Mater.* 2014; 13: 125-38.
41. Kircher MF, Gambhir SS, Grimm J. Noninvasive cell-tracking methods. *Nat Rev Clin Oncol.* 2011; 8: 677-88.
42. Ottobrini L, Martelli C, Trabattini DL, Clerici M, Lucignani G. *In vivo* imaging of immune cell trafficking in cancer. *Eur J Nucl Med Mol Imaging.* 2011; 38: 949-68.
43. Bergenfelz C, Larsson AM, von Stedingk K, Gruvberger-Saal S, Aaltonen K, Jansson S, et al. Systemic Monocytic-MDSCs Are Generated from Monocytes and Correlate with Disease Progression in Breast Cancer Patients. *PLoS One.* 2015; 10: e0127028.
44. Jordan KR, Amaria RN, Ramirez O, Callihan EB, Gao D, Borakove M, et al. Myeloid-derived suppressor cells are associated with disease progression and decreased overall survival in advanced-stage melanoma patients. *Cancer Immunol Immunother.* 2013; 62: 1711-22.
45. Toh B, Wang X, Keeble J, Sim WJ, Khoo K, Wong WC, et al. Mesenchymal transition and dissemination of cancer cells is driven by myeloid-derived suppressor cells infiltrating the primary tumor. *PLoS Biol.* 2011; 9: e1001162.
46. Basu S, Hodgson G, Katz M, Dunn AR. Evaluation of role of G-CSF in the production, survival, and release of neutrophils from bone marrow into circulation. *Blood.* 2002; 100: 854-61.
47. Movahedi K, Laoui D, Gysemans C, Baeten M, Stangé G, Van den Bossche J, et al. Different Tumor Microenvironments Contain Functionally Distinct Subsets of Macrophages Derived from Ly6C(high) Monocytes. *Cancer Res.* 2010; 70: 5728-39.
48. Condamine T, Ramachandran I, Youn J-I, Gabrilovich DI. Regulation of tumor metastasis by myeloid-derived suppressor cells. *Annu Rev Med.* 2015; 66: 97-110.
49. Gao D, Joshi N, Choi H, Ryu S, Hahn M, Catena R, et al. Myeloid progenitor cells in the premetastatic lung promote metastases by inducing mesenchymal to epithelial transition. *Cancer Res.* 2012; 72: 1384-94.
50. Umansky V, Sevko A, Gebhardt C, Utikal J. Myeloid-derived suppressor cells in malignant melanoma. *J Dtsch Dermatol Ges.* 2014; 12: 1021-7.
51. Poschke I, Mougiakakos D, Hansson J, Masucci GV, Kiessling R. Immature immunosuppressive CD14+HLA-DR-/low cells in melanoma patients are Stat3hi and overexpress CD80, CD83, and DC-sign. *Cancer Res.* 2010; 70: 4335-45.
52. Pico de Coana Y, Poschke I, Gentilcore G, Mao Y, Nystrom M, Hansson J, et al. Ipilimumab treatment results in an early decrease in the frequency of circulating granulocytic myeloid-derived suppressor cells as well as their Arginase1 production. *Cancer Immunol Res.* 2013; 1: 158-62.
53. Highfill SL, Cui Y, Giles AJ, Smith JP, Zhang H, Morse E, et al. Disruption of CXCR2-mediated MDSC tumor trafficking enhances anti-PD1 efficacy. *Sci Transl Med.* 2014; 6: 237ra67.
54. Meyer C, Cagnon L, Costa-Nunes CM, Baumgaertner P, Montandon N, Leyvraz L, et al. Frequencies of circulating MDSC correlate with clinical outcome of melanoma patients treated with ipilimumab. *Cancer Immunol Immunother.* 2014; 63: 247-57.
55. Draghiciu O, Lubbers J, Nijman HW, Daemen T. Myeloid derived suppressor cells-An overview of combat strategies to increase immunotherapy efficacy. *Oncoimmunology.* 2015; 4: e954829.
56. Suzuki E, Kapoor V, Jassar AS, Kaiser LR, Albelda SM. Gemcitabine selectively eliminates splenic Gr-1<sup>+</sup>/CD11b<sup>+</sup> myeloid suppressor cells in tumor-bearing animals and enhances antitumor immune activity. *Clin Cancer Res.* 2005; 11: 6713-21.
57. Vincent J, Mignot G, Chalmin F, Ladoire S, Bruchard M, Chevriaux A, et al. 5-Fluorouracil selectively kills tumor-associated myeloid-derived suppressor cells resulting in enhanced T cell-dependent antitumor immunity. *Cancer Res.* 2010; 70: 3052-61.
58. Sierra RA, Trillo-Tinoco J, Mohamed E, Yu L, Achyut BR, Arbab A, et al. Anti-Jagged Immunotherapy Inhibits MDSCs and Overcomes Tumor-Induced Tolerance. *Cancer Res.* 2017; 77: 5628-38.
59. Orillion A, Hashimoto A, Damayanti N, Shen L, Adelaiye-Ogala R, Arisa S, et al. Entinostat Neutralizes Myeloid-Derived Suppressor Cells and Enhances the Antitumor Effect of PD-1 Inhibition in Murine Models of Lung and Renal Cell Carcinoma. *Clin Cancer Res.* 2017; 23: 5187-201.
60. Kim K, Skora AD, Li Z, Liu Q, Tam AJ, Blosser RL, et al. Eradication of metastatic mouse cancers resistant to immune checkpoint blockade by suppression of myeloid-derived cells. *Proc Natl Acad Sci U S A.* 2014; 111: 11774-9.